NASA CR-165350

SSS-R-81-4847

ADDITIONAL APPLICATION OF THE NASCAP CODE

VOLUME II: SEPS, ION THRUSTER NEUTRALIZATION AND ELECTROSTATIC ANTENNA MODEL

I. Katz, J.J. Cassidy, M.J. Mandell, D.E. Parks,

G.W. Schnuelle, P.R. Stannard, P.G. Steen

SYSTEMS, SCIENCE AND SOFTWARE

Prepared for

NATIONAL AERONAUTICS AND SPACE ADMINISTRATION

NASA LEWIS RESEARCH CENTER

Contract NAS3-21762

1. Report No.	2. Government Accession No.	3. Recipient's Catalog No.
NASA CR-165350		

4. Title and Subtitle	5. Report Date
ADDITIONAL APPLICATION OF THE NASCAP CODE, VOLUME II: SEPS, ION THRUSTER NEUTRALIZATION AND ELECTROSTATIC ANTENNA MODELS	February 1981
	6. Performing Organization Code
7. Author(s)	8. Performing Organization Report No.
I. Katz, J. J. Cassidy, M. J. Mandell, D. E. Parks, G. W. Schnuelle, P. R. Stannard, P. G. Steen	SSS-R-81-4847 (Vol. II)
	10. Work Unit No.
9. Performing Organization Name and Address	11. Contract or Grant No.
Systems, Science and Software P. O. Box 1620 La Jolla, CA 92038	NAS3-21762
	13. Type of Report and Period Covered
12. Sponsoring Agency Name and Address	Contractor Report 3/1979-10/1980
National Aeronautics and Space Administration Lewis Research Center 21000 Brookpark Road, Cleveland, OH 44135	14. Sponsoring Agency Code
	5532

15. Supplementary Notes

Project Manager, James C. Roche, NASA-Lewis Research Center, Cleveland, OH

16. Abstract

The interactions of spacecraft systems with the surrounding plasma environment have been studied analytically for three cases of current interest. These studies include calculating the impact of spacecraft generated plasmas on the main power system of a baseline Solar Electric Propulsion Stage (SEPS), the modeling of the physics of the neutralization of an ion thruster beam by a plasma bridge, and examining the physical and electrical effects of orbital ambient plasmas on the operation of an electrostatically controlled membrane mirror. In order to perform these studies use was made of the NASA Charging Analyzer Program (NASCAP), as well as several other computer models and analytical estimates. The main result of the SEPS study was to show how charge exchange ion expansion can create a conducting channel between the thrusters and the solar arrays. A new fluid-like model was able to predict plasma potentials and temperatures measured near the main beam of an ion thruster and in the vicinity of a hollow cathode neutralizer. Power losses due to plasma currents were shown to be substantial for several proposed electrostatic antenna designs.

17. Key Words (Suggested by Author(s))	18. Distribution Statement
Solar Electric Propulsion, SEPS, Ion Thruster, Ion Engine, Hollow Cathode Neutralizer, Parasitic Currents, Electrostatic Antenna, Large Space Structure, Space Based Antenna, Electrostatically Controlled Membrane Mirror	Publicly Available

19. Security Classif. (of this report)	20. Security Classif. (of this page)	21. No. of Pages	22. Price*
Unclassified	Unclassified	115	

* For sale by the National Technical Information Service, Springfield, Virginia 22161

TABLE OF CONTENTS

TABLE OF CONTENTS (Continued)

LIST OF FIGURES

LIST OF FIGURES (Continued)

LIST OF TABLES

SUMMARY

The interactions of spacecraft systems with the surrounding plasma environment have been studied analytically for three cases of current interest. These studies include calculating the impact of spacecraft generated plasmas on the main power system of a baseline Solar Electric Propulsion Stage (SEPS), the modeling of the physics of the neutralization of an ion thruster beam by a plasma bridge, and examining the physical and electrical effects of orbital ambient plasmas on the operation of an electrostatically controlled membrane mirror. In order to perform these studies use was made of the NASA Charging Analyzer Program (NASCAP), as well as several other computer models and analytical estimates. The main result of the SEPS study was to show how charge exchange ion expansion can create a conducting channel between the thrusters and the solar arrays. A new fluid-like model was able to predict plasma potentials and temperatures measured near the main beam of an ion thruster and in the vicinity of a hollow cathode neutralizer. Power losses due to plasma currents were shown to be substantial for several proposed electrostatic antenna designs.

1. INTRODUCTION

This is the Final Report on Tasks 1, 2, and 3 of Contract NAS3-21762, "Additional Application of the NASCAP Code". The work was performed by Systems, Science and Software between 26 March 1979 and 9 October 1980.

Much of the material contained in this final report was published previously in topical, monthly, and conference reports. Produced separately under this contract are two other final reports. One describes NASCAP extensions[1] including the new Low Earth Orbit (LEO) model. The other provides a detailed analysis of the SCATHA spacecraft. Other relevant NASCAP documents include "A Three Dimensional Dynamic Study of Electrostatic Charging in Materials," NASA CR-135256, and "NASCAP User's Manual," NASA CR-135259.

The interaction of ion engine generated plasmas with spacecraft systems is a problem fundamental to the development of a Solar Electric Propulsion Stage (SEPS). In Chapter 2 we present a complex multidimensional analysis of charge exchange ion expansion and interaction with solar panels. The calculations indicate possible difficulties with the use of high voltages on the arrays.

The major technical accomplishment under this contract has been the development of a workable theory of ion engine neutralization. In Chapter 3 and Appendix A, a fluid-like model of electron flow is described along with the results of two test calculations. The agreement with experiment is compelling evidence of fluid-like behavior.

The last study, contained in Chapter 4, is detailed analytical investigation of environmental interactions of the electrostatic antenna baseline design. Included are spacecraft charging, electromechanical, parasitic current,

and sputtering investigations. The primary area of importance again turns out to be power drain in low earth orbit due to current paths through the dense ambient plasma.

2. PARASITIC CURRENT LOSSES DUE TO SOLAR ELECTRIC PROPULSION GENERATED PLASMAS

2.1 INTRODUCTION

Solar electric propulsion is a leading candidate for lifting large structures from shuttle orbit to geostationary altitude. A previous study[2] demonstrated that plasma produced by charge-exchange reactions within the ion beam may dominate the ambient environment near the spacecraft. The ad hoc nature of the previous work made clear the need for a more accurate treatment of the expansion of the charge-exchange plasma and the resultant solar array power losses. The calculations presented here are an improvement over previous work in that they contain a predictive model for the charge-exchange plasma expansion, and a fully three-dimensional model for the structure of the plasma sheath around the solar array wing.

For this study we have considered a 30 cm diameter mercury thruster producing 2 A of beam current and 25 mA of charge-exchange current. The charge-exchange ions are emitted radially, with energies of 5-10 eV, in the first thruster diameter of the beam. This gives a density of $\sim 2.5 \times 10^{14}$ m^{-3} at the beam edge, which exceeds the LEO plasma density of 10^{10}-10^{12} m^{-3}. Thus the charge-exchange plasma will dominate the ambient to a distance of several meters from the thruster in LEO, and over the entire spacecraft for substantially more tenuous environments.

The conditions in this plasma are long collision lengths ($\sim 10^{3}$ m) and short Debye lengths ($\sim 10^{-3}$ m). In this regime we assume that the electron plasma adjusts itself to maintain isothermal, quasi-neutral conditions. This implies a barometric law potential,

$$\phi = \theta \ell n (n/n_A) \qquad (2.1)$$

where θ is the electron temperature (eV), n the local plasma density, and n_A the ambient plasma density. This potential causes expansion and diffusion of the ion cloud as it emerges from the beam edge. Far downstream the electrostatic force become small, so that the ion density takes the form $f(\theta)/r^2$, where θ is the polar angle relative to the beam and r the distance from the engine.

The ion plasma is modeled hydrodynamically, i.e., we assume the ion density and velocity to be a well-defined function of position, and the ion thermal motion to be unimportant. The motion then satisfies the equations of continuity of mass and momentum:

$$\frac{\partial \rho}{\partial t} = -\underset{\sim}{\nabla} \cdot (\rho \underset{\sim}{v}) \tag{2.2}$$

$$\frac{\partial}{\partial t} (\rho v_\alpha) = -\underset{\sim}{\nabla} \cdot (v_\alpha \rho \underset{\sim}{v}) + \frac{\rho e E_\alpha}{m} \tag{2.3}$$

where subscript α denotes a Cartesian component, and E is the electric field. The challenge is to develop numerical methods capable of finding the steady-state solution to Eqs. (2.1-2.3) in the R-Z (cylindrical) geometry appropriate to the problem.

2.2 NUMERICAL METHODS

We solve the problem on the computational mesh shown in Figure 2.1. The physical space is located within the solid boundary; mesh points outside the physical space are computationally convenient and serve to maintain boundary conditions. Velocities are defined at the points indicated by crosses, which form an evenly spaced r-z mesh:

$$r_i^{(v)} = r_o + i\,\Delta r \tag{2.4a}$$

$$z_j^{(v)} = z_o + j\,\Delta z \tag{2.4b}$$

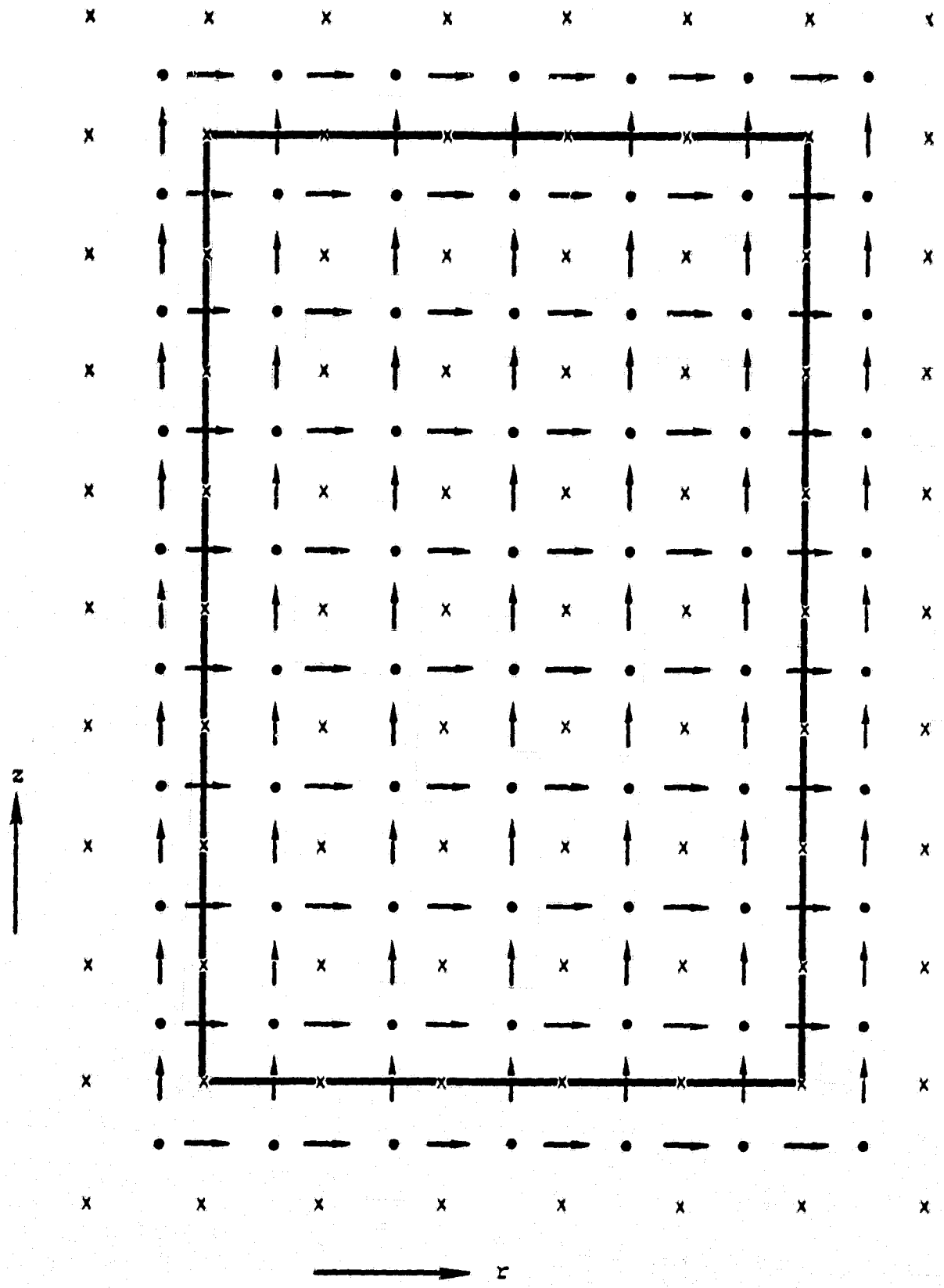

Figure 2.1. Computational space, showing points for definition of velocity (x), density (•), and mass flux (→).

Densities are defined at the centroids of the quadrilaterals formed by the crosses:

$$r_i^{(\rho)2} = \frac{1}{2}\left(r_i^{(v)2} + r_{i+1}^{(v)2}\right) \tag{2.5a}$$

$$z_j^{(\rho)} = \frac{1}{2}\left(z_j^{(v)} + z_{j+1}^{(v)}\right) \tag{2.5b}$$

Mass fluxes, $\underset{\sim}{f}$, are defined at the arrows in a fully "upwind" sense:

$$v_r\left(r_i^{(v)}, z_j^{(\rho)}\right) = \frac{1}{2}\left[v_r\left(r_i^{(v)}, z_j^{(v)}\right) + v_r\left(r_i^{(v)}, z_{j+1}^{(v)}\right)\right] \tag{2.6a}$$

$$(\Delta r) v_z\left(r_i^{(\rho)}, z_j^{(v)}\right) = \left(r_{i+1}^{(v)} - r_i^{(\rho)}\right) v_z\left(r_i^{(v)}, z_j^{(r)}\right) + \left(r_i^{(\rho)} - r_i^{(v)}\right) v_z\left(r_{i+1}^{(v)}, z_j^{(v)}\right) \tag{2.6b}$$

$$f_r\left(r_i^{(v)}, z_j^{(\rho)}\right) = \left(r_k^{(\rho)} / r_i^{(v)}\right) \rho\left(r_k^{(\rho)}, z_j^{(\rho)}\right) v_r\left(r_i^{(v)}, z_j^{(\rho)}\right)$$

$$k = \begin{cases} i-1 & \text{if } v_r \geq 0 \\ i & \text{if } v_r < 0 \end{cases} \tag{2.6c}$$

$$f_z\left(r_i^{(\rho)}, z_j^{(v)}\right) = \rho\left(r_i^{(\rho)}, z_\ell^{(\rho)}\right) v_z\left(r_i^{(\rho)}, z_j^{(v)}\right)$$

$$\ell = \begin{cases} j-1 & \text{if } v_z \geq 0 \\ j & \text{if } v_z < 0 \end{cases} \tag{2.6d}$$

With above definitions, it is straightforward to timestep the integral form of Eq. (2.2), using as control volumes the rectangles formed by the four crosses (velocity definition points) surrounding a density definition point.

Equation (2.3) is then used to construct $d\vec{v}/dt$. We use a finite difference method to evaluate the divergence term as follows:

a. Define mass fluxes flowing between the crosses in Figure 2.1, i.e., normal to the arrows. This is done by taking weighted averages of nearby already defined fluxes:

$$4r_i^{(\rho)} f_r\left(r_i^{(\rho)}, z_j^{(v)}\right) = \sum_{k=1}^{i+1} \sum_{\ell=j-1}^{j} r_k^{(v)} f_r\left(r_k^{(v)}, z_\ell^{(\rho)}\right) \qquad (2.7)$$

$$4r_i^{(v)} f_z\left(r_i^{(v)}, z_j^{(\rho)}\right) = \sum_{k=i-1}^{i} \sum_{\ell=j}^{j+1} r_k^{(\rho)} f_z\left(r_k^{(\rho)}, z_\ell^{(v)}\right) \qquad (2.8)$$

b. Define densities associated with velocity definition points:

$$4r_i^{(v)} \rho\left(r_i^{(v)}, z_j^{(v)}\right) = \sum_{k=i-1}^{i} \sum_{\ell=j-1}^{j} r_k^{(\rho)} \rho\left(r_k^{(\rho)}, z_\ell^{(\rho)}\right) \qquad (2.9)$$

These densities are needed at both their previous and current (just updated) values.

c. Define velocities at the arrows:

$$\left(r_{i+1}^{(v)} - r_i^{(v)}\right) \underset{\sim}{v}\left(r_i^{(\rho)}, z_j^{(v)}\right) = \left(r_i^{(\rho)} - r_i^{(v)}\right) \underset{\sim}{v}\left(r_{i+1}^{(v)}, z_j^{(v)}\right) + \left(r_{i+1}^{(v)} - r_i^{(\rho)}\right) \underset{\sim}{v}\left(r_i^{(v)}, z_j^{(v)}\right)$$

$$\left(z_{j+1}^{(v)} - z_j^{(v)}\right) \underset{\sim}{v}\left(r_i^{(v)}, z_j^{(\rho)}\right) = \left(z_j^{(\rho)} - z_j^{(v)}\right) \underset{\sim}{v}\left(r_i^{(v)}, z_{j+1}^{(\rho)}\right) + \left(z_{j+1}^{(v)} - z_j^{(\rho)}\right) \underset{\sim}{v}\left(r_i^{(v)}, z_j^{(\rho)}\right)$$

d. Determine the change in velocity by

$$\Omega_{ij} \frac{d}{dt}\left[\rho\left(r_i^{(v)}, z_j^{(v)}\right) \underset{\sim}{v}\left(r_i^{(v)}, z_j^{(v)}\right)\right] = -\sum_k S_k\left(\hat{n}_k \cdot \underset{\sim}{f}_k\right) \underset{\sim}{v}_k + \Omega_{ij} \underset{\sim}{F}_{ij}$$

where Ω_{ij} is the volume

$$r_{i-1}^{(\rho)} < r < r_i^{(\rho)};\ z_{i-1}^{(\rho)} < z < z_i^{(\rho)} ,$$

S_k are the surfaces bounding that volume, and $\underset{\sim}{F}_{ij}$ is the force at $\left(r_i^{(v)}, z_j^{(v)}\right)$. Specifically

$$\Omega_{ij} = \pi\left(r_i^{(\rho)2} - r_{i-1}^{(\rho)2}\right)\left(z_i^{(\rho)} - z_{i-1}^{(\rho)}\right)$$

$$- \sum_k S_k\left(\hat{n}_k \cdot \underset{\sim}{f}_k\right)\underset{\sim}{v}_k$$

$$= 2\pi\left(z_i^{(\rho)} - z_{i-1}^{(\rho)}\right)\left[r_{i-1}^{(\rho)}\, f_r\left(r_{i-1}^{(\rho)}, z_i^{(v)}\right)\underset{\sim}{v}\left(r_{i-1}^{(\rho)}, z_i^{(v)}\right)\right.$$

$$\left. - r_i^{(\rho)}\, f_r\left(r_i^{(\rho)}, z_i^{(v)}\right)\underset{\sim}{v}\left(r_{i-1}^{(\rho)}, z_i^{(v)}\right)\right]$$

$$+ \pi\left(r_i^{(\rho)2} - r_{i-1}^{(\rho)2}\right)\left[f_z\left(r_i^{(v)}, z_{i-1}^{(\rho)}\right)\underset{\sim}{v}\left(r_i^{(v)}, z_{i-1}^{(\rho)}\right)\right.$$

$$\left. - f_z\left(r_i^{(v)}, z_i^{(\rho)}\right)\underset{\sim}{v}\left(r_i^{(v)}, z_i^{(\rho)}\right)\right]$$

$$\underset{\sim}{v}_{ij}(t) = \rho_{ij}(t-dt)\,\underset{\sim}{v}_{ij}(t-dt)/\rho_{ij}(t) + \underset{\sim}{a}_{ij}(t)\,dt$$

$$- \frac{dt}{\Omega_{ij}\rho_{ij}(t)} \sum_k S_k\left(\hat{n}_k \cdot \underset{\sim}{f}_k\right)\underset{\sim}{v}_k \;;$$

$$a_{ij}(t) = (e/m)\,\underset{\sim}{E}\left(r_i^{(v)}, z_j^{(v)}\right) .$$

These formulae are accurate to first order in dt and second order in (dr,dz).

e. Additionally, provision is made for some velocity smoothing at each timestep.

2.3 RESULTS

As an example, we calculated the expansion of an ion plume with initial conditions similar to a case measured by Hughes Research Laboratory.[3] The initial conditions were:

Emission energy (radial) = 10 eV.

Initial radius $r_1^{(v)} = .15$ m.

Current density $e\,\rho\left(r_1^{(v)},z\right)\,v_r\left(r_2^{(v)},z\right)$

$$= \begin{cases} 0 & z < 0 \\ .123\,\exp(-z/.22) & z > 0 \end{cases}$$

(total current = 25 mA)

Electron temperature $\theta_e = 1$ eV.

Mass (Hg ion) = 3.34×10^{-25} kg.

Ambient density $n_A = 10^{12}\ m^{-3}$.

It follows that

$$v_r\left(r_1^{(v)},z\right) = 3095 \text{ m/sec}$$

$$\rho\left(r_1^{(v)},0\right) = 2.48 \times 10^{14}\ m^{-3}$$

$$\phi_{max} = \theta\rho\ell n\left[\rho\left(r_i^{(v)},0\right)/n_A\right] = 5.5 \text{ V.}$$

The calculation was done in three phases:

a. $.15 \text{ m} < r < 1.15 \text{ m};\ \Delta r = 0.05 \text{ m}$
$-1.0 \text{ m} < z < 1.0 \text{ m};\ \Delta z = 0.10 \text{ m}$

b. $1.0 \text{ m} < r < 5.0 \text{ m};\ \Delta r = 0.2 \text{ m}$
$-2.0 \text{ m} < z < 2.0 \text{ m};\ \Delta z = 0.2 \text{ m}$

c. $2.0 \text{ m} < r < 12 \text{ m};\ \Delta r = 0.5 \text{ m}$
$-4.0 \text{ m} < z < 4 \text{ m};\ \Delta z = 0.4 \text{ m}$

Initial conditions for the second and third phases were obtained by interpolating data from the previous phase and renormalizing to retain the correct total current. At each phase, the calculation was carried out until steady-state densities and velocities were reached.

The results are shown in Figures 2.2 and 2.3. It is seen that the initially asymmetric expansion (Figure 2.2) becomes roughly spherical by a radius of $\sim$1 m from the beam. This is seen in Figure 2.3a, in which spherical $(r^2 + z^2)$ scaling maintains constant arrow length, and in Figure 2.3b, which indicates radial contours of equal density. The density (m^{-3}) beyond 1 m from the engine is reasonably approximated by

$$\rho \approx 10^{13} \ (\sin\theta)^{12}/(r^2 + z^2)$$

where θ is the angle from the beam direction. A closer inspection of Figure 2.3b indicates that the plume extends further upstream than downstream. This is attributable to "pressure blowoff" at the upstream plume edge near the engine where the density gradient is high.

The plasma parameters determined from the above model are used as input to a fully three-dimensional computer program designed to predict current collection by high voltages in low temperature, short Debye length plasmas.[4,5] This model uses an analytic, nonlinear space charge formulation, correct in both Debye screening and thin sheath limits, to determine the electrostatic potential and the boundary of the plasma sheath. The model allows the plasma temperature and density to vary in space. Figure 2.4 gives a sample of electrostatic potential contours near a solar array wing, illustrating the asymmetry caused by the charge-exchange plasma being predominantly on one side of the wing. By

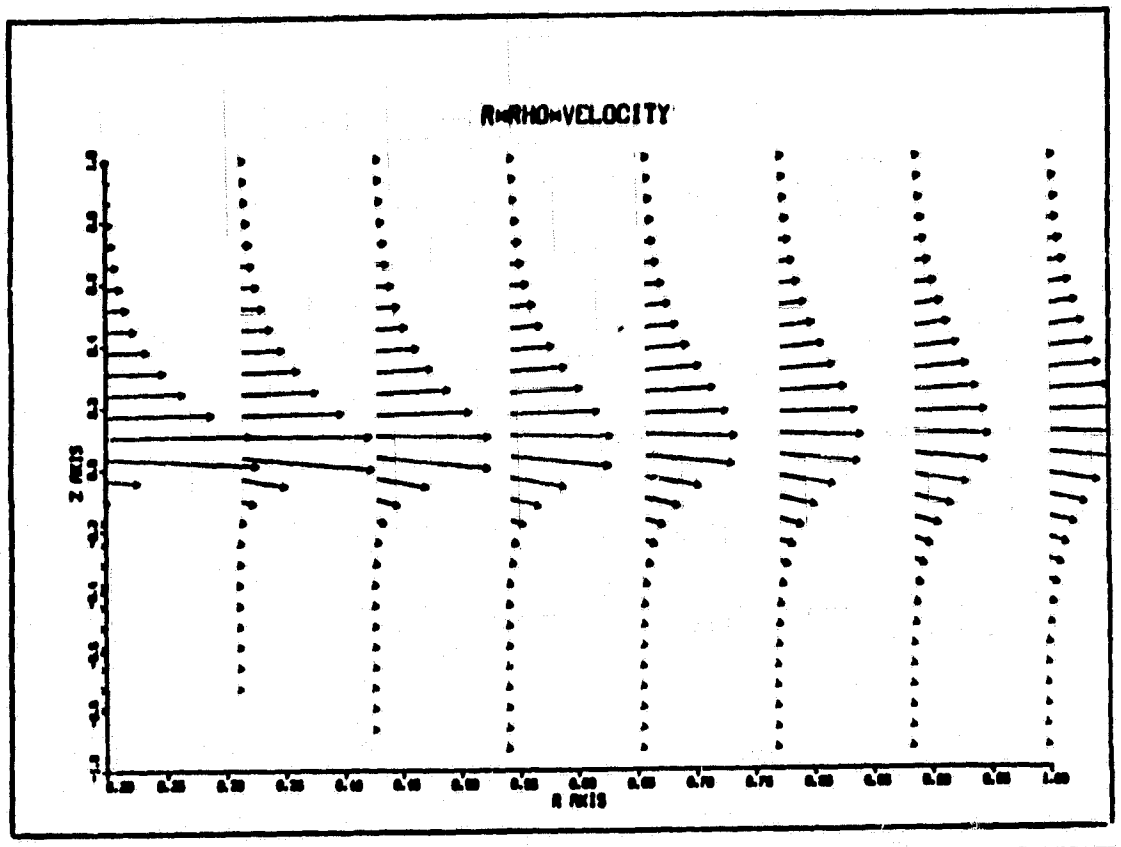

(a)

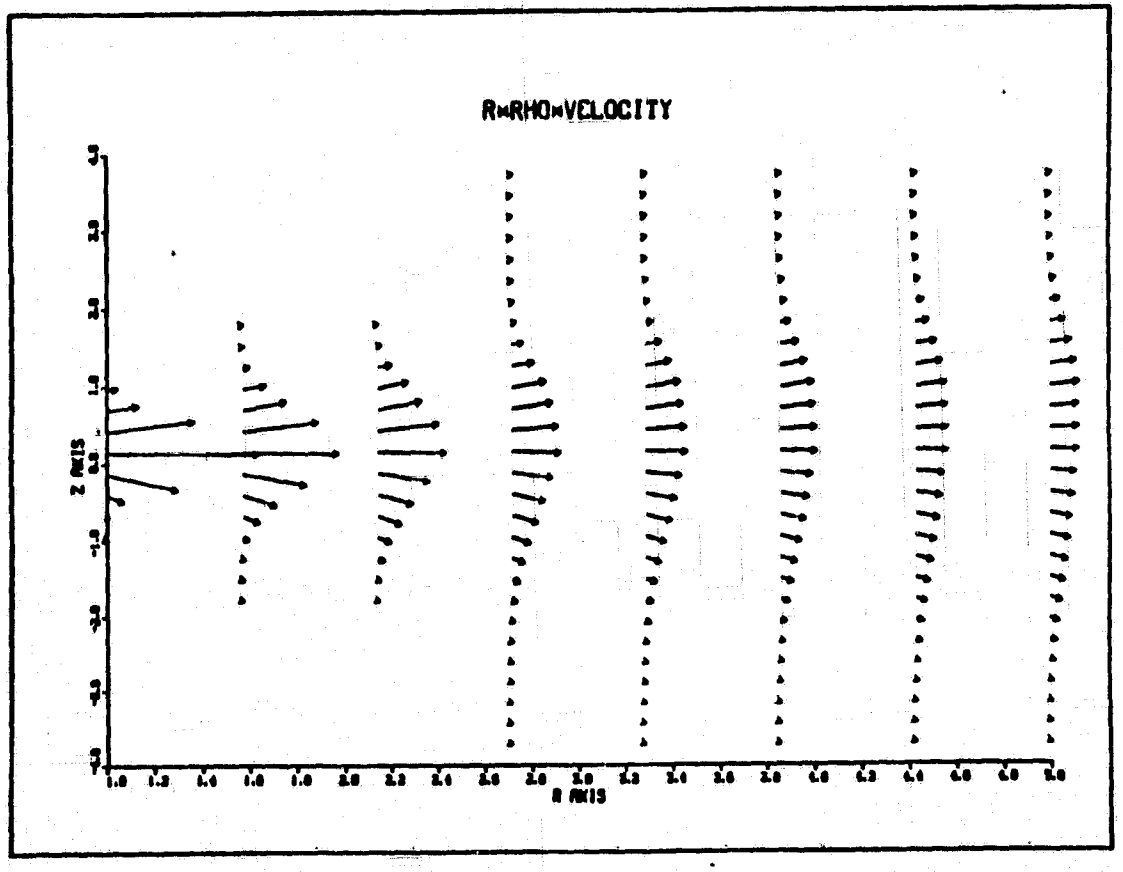

(b)

Figure 2.2. Cylindrically scaled current density plots for ion plume flow (a) near the beam, and (b) in the "spherical expansion" region.

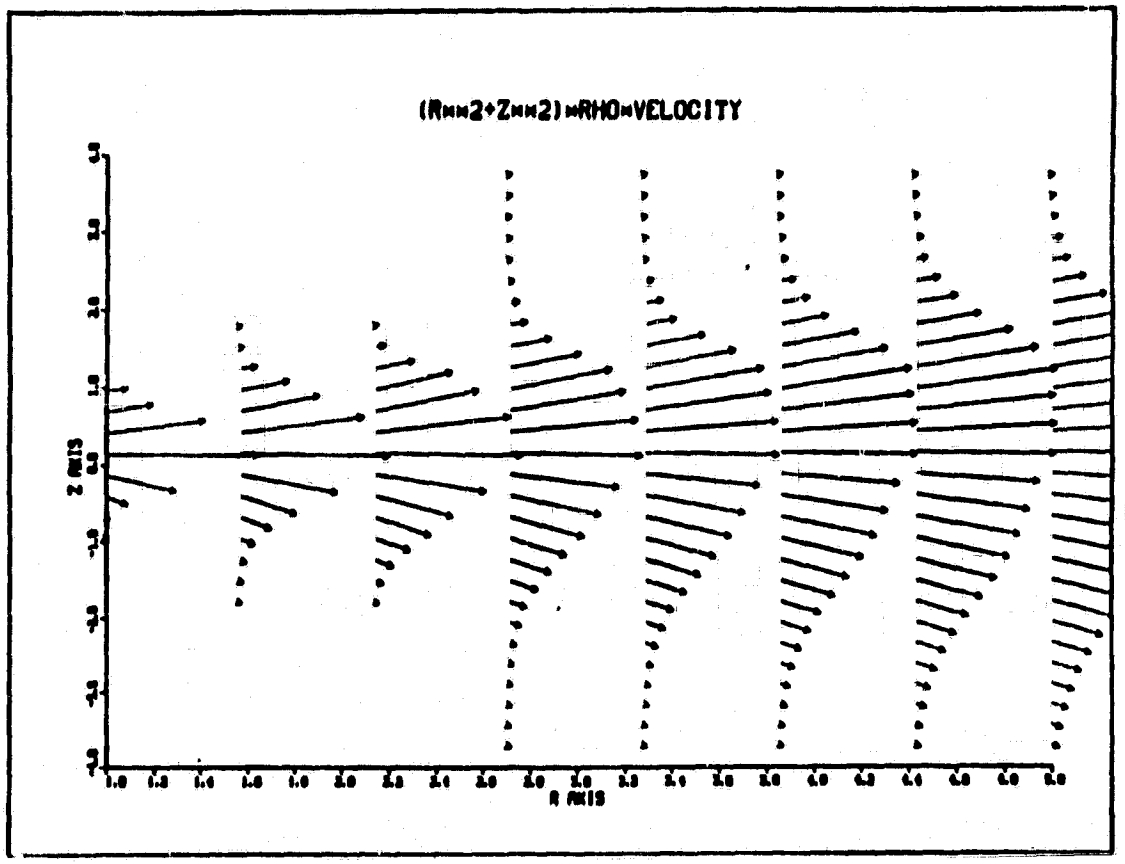

(a)

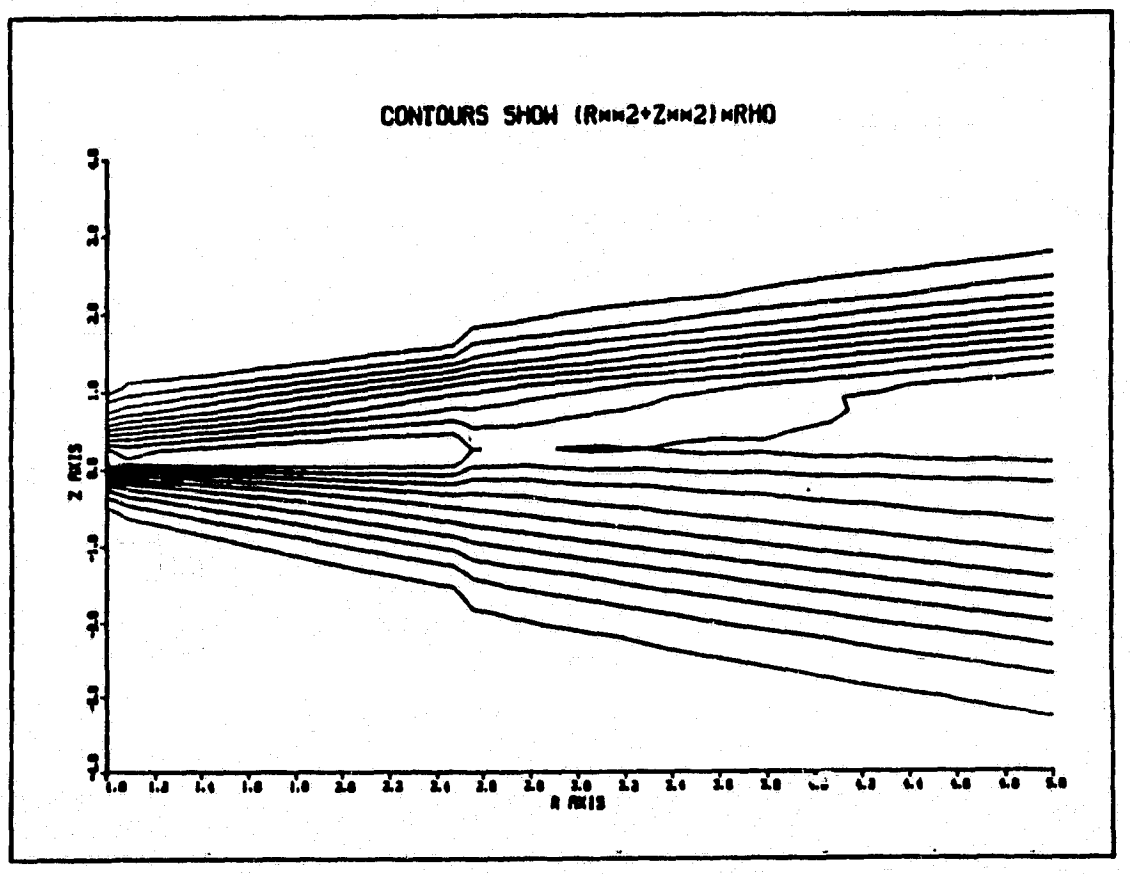

(b)

Figure 2.3. Spherically scaled plots of (a) current density and (b) particle density contours.

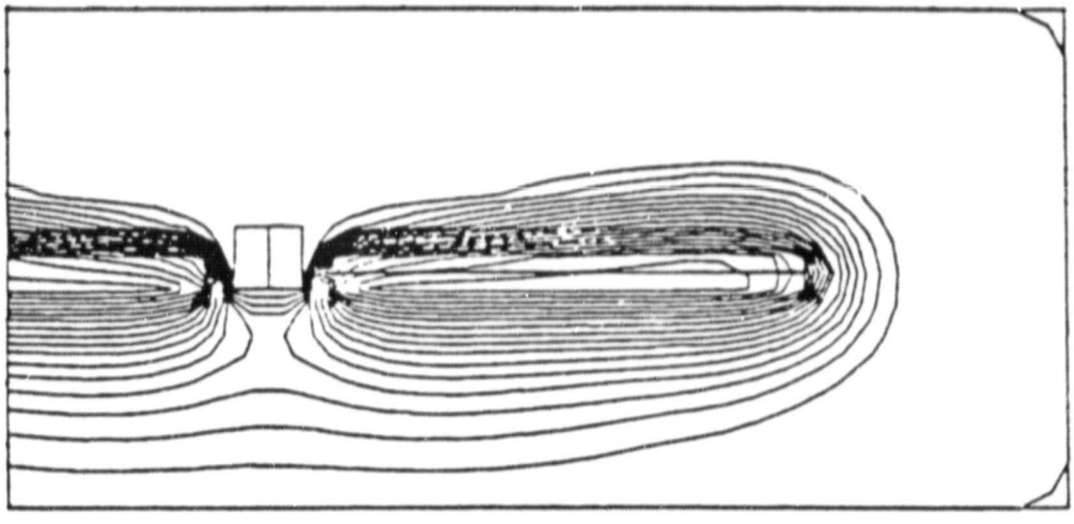

Figure 2.4. Potential contours about a 2 kV solar array in the presence of the charge exchange plume. Note that the potential is more shielded above the wing (where the charge exchange plasma is located) than below.

tracking electrons inward from the sheath boundary, good parasitic current estimates are obtained. Iterating on the two stages of the calculation allows non-local effects to be included. Additionally, a high resolution capability is available to compute the current distribution over a complex pattern of solar cells.

Table 2.1 gives sample results for an 8 m × 30 m, 25 kw solar array for several orientations and configurations. In these calculations, the spacecraft body was held at plasma ground and the solar cells were positively biased. Parasitic currents to both sides of each 10 m section of the wing were separately monitored. Several trends are apparent: (1) The inboard section of the wing draws most of the current, even though it is at a low voltage. This is because of the r^{-2} expansion of the charge-exchange plasma. (2) The current to the outboard section is similar to the center section current, due to the large end effect in the tenuous plasma. (3) When the beam is in the plane of the panel, an increased loss is caused by the array's intersecting the charge-exchange pancake. It is apparent from these results that with kilovolt biases power losses of ∿10 percent or more are likely, even with only one engine in operation, and that ameliorative measures should focus on the inboard portion of the solar arrays.

Table 2.1. Power Losses for 8m×30m Solar Array for One Thruster and Various Configurations.

Configuration	Voltage			Current (one side)			Power Loss
	Inboard	Center	Outboard	Inboard	Center	Outboard	(per wing)
a,d	1000	2000	3000	1.4	0.6	0.6	4.4
b,d	2000	2000	2000	4.7	0.6	0.5	12.0
b,d	1000	2000	3000	3.7	0.6	0.5	6.4
a,c	1000	2000	3000	1.1	0.3	0.4	5.9
a,c	100	1000	2000	0.8	0.3	0.4	2.3
a,d	200	200	200	1.4	0.3	0.2	0.38
a,d	400	400	400	1.5	0.3	0.3	0.85

a - Beam in plane of panel
b - Beam normal to plane of panel
c - Both sides biased
d - Back of panel grounded

All voltages in volts, currents in amps, and power losses in kilowatts.

3. ION ENGINE NEUTRALIZER STUDY

3.1 PHYSICAL MODEL

The purpose of the present investigation is to determine if simple models for electron transport give qualitatively correct predictions of the plasma properties in the vicinity of an ion thruster.

Within a meter or so of the ion thruster, the electron densities are in the range

$$10^8 \lesssim n \lesssim 10^{13} \text{ cm}^{-3}$$

and their velocity distribution is characterized by temperature Θ between about one and ten electron volts. The Debye length

$$\lambda_D \simeq 700 \sqrt{\frac{\Theta}{n}} \text{ cm}$$

is typically small compared to distances L over which there is a substantial variation of macroscopic plasma properties such as density, potential, and temperatures. On the other hand, the mean free path for pair collisions

$$\lambda_c \simeq 10^{12} E^{1/2} \Theta^{1/2}/n \text{ cm}, \quad E \lesssim \Theta$$

for electrons of energy E (eV) is typically long compared to L, so that the behavior of the plasma is controlled by collective rather than collisional effects. Since $\lambda_D \ll L$, the plasma is quasineutral, departures from neutrality amounting roughly to

$$\delta n/n \sim \left(\frac{\lambda_D}{L}\right)^2 \sim 10^{-4} ,$$

the space around the vehicle is strongly shielded from surface

potentials. This is in contrast to the situation that prevails in charging of spacecraft in geosynchronous orbit where effects of space charge are entirely negligible and potentials are determined as solutions of Laplace's equation.

Although collisionless, thruster-generated plasmas exhibit macroscopic behavior similar in many respects to that of a collisional plasma. Such behavior is perhaps not totally unexpected in view of the fact that in both non-equilibrium and equilibrium plasmas electrons are scattered by fluctuating electric fields. A primary difference between the equilibrium and non-equilibrium cases is in the magnitude of the fluctuating fields.

Several investigators have measured properties of thruster generated plasmas.[6-9] In the experiments of Ogawa, et al., on cesium ion beams neutralized by electrons from a hot wire, measurements were made of the density, potential, and electron temperature in the beam plasma. The potential difference between the neutralizer wire and the plasma could be varied by changing the position of the wire, the large potential differences (electron injection voltages) occurring when the wire was completely withdrawn from the beam plasma. An important result of the Ogawa experiments was that over a wide range of conditions electron density n and plasma potential ϕ were well correlated by the barometric law

$$n(\vec{r}) = \text{const} \exp(q\phi(\vec{r})/kT) \tag{3.1}$$

where T is the electron temperature. The approximate validity of the barometric law was further verified by Kaufman.[10]

Since the barometric law is a thermal equilibrium concept, it can be completely valid only if the plasma is isothermal. The plasma is only approximately isothermal, noticeable deviation occurring as one proceeds from the beam axis beyond the beam edge into the plasma formed by ambient and charge exchange ions. Kaufman observes an electron temperature in the charge exchange plasma only about half that in the beam.[9] Ogawa[8] and Sellen[6] obtained measurable temperature variations in the beam plasma over several tens of centimeters in the downstream direction from the accelerator grid. The largest deviations from the barometric law were observed for large injection potentials ($\gtrsim$10 volts). Probe traces in such cases also indicated departures of the electron spectrum from a Maxwellian shape.

Probe measurements of the plasma potential in the thruster beam were made in SERT II flight and ground test experiments. The measurements show strong variation of plasma potential across the beam boundary about 20 cm downstream from the thruster grids. Such results are difficult to explain on the basis of a barometric law relationship unless the electron temperature or density variation from beam center to beam edge is much higher than might be expected from other measurements made in similar configurations. We anticipate, however, that such is not the case and, instead, that the observed behavior should be explained in terms of the anomolous resistivity of the thruster generated plasma to the flow of electron current. Thus, the primary objective of the following sections of this chapter is to determine the capability of simple transport models to explain, at least qualitatively, the experimental results.

We first give the precise kinetic equation for the electron distribution and the first few moment equations expressing conservation of change, momentum, and energy. From there, we state the approximations leading to the transport equation which we eventually solve. The method of solution and the results of calculations will be the subject of a later report.

Exact Equation

In principle, a kinetic approach based on the Vlasov-Boltzmann equation fully describes the spacecraft generated plasma. The complexity of such an approach, however, makes it impractical as a basis for conducting multidimensional calculations of plasma behavior. Besides, except near sources and collecting surfaces, where the distribution function may change markedly, one should be able to adequately describe the plasma in terms of certain average properties of the distribution, such as temperature, density, and particle and heat fluxes.

Quite generally the state of the plasma can be specified by the distribution function $\vec{f}_a(\vec{r},\vec{v},t)$ that characterize each particle component a, where $f_a(\vec{r},\vec{v},t)d\vec{r}\,d\vec{v}$ represents the number of particles of species a in the six dimensional volume element $d\vec{r}\,d\vec{v}$ about the position $\vec{r},\vec{v}$ in phase space. The kinetic equations which describe the distribution are

$$\frac{\partial f_a}{\partial t} + \vec{v}\cdot\nabla f_a + \frac{\vec{F}_a}{m_a}\cdot\nabla_v f_a = C_a \qquad (3.2)$$

For particles of mass m_a and charge q_a in an electric field $\vec{E}$ and a magnetic field $\vec{B}$ the "smoothed" force on a particle is

$$\vec{F}_a = q_a \left(\vec{E} + \frac{\vec{V} \times \vec{B}}{c} \right) \tag{3.3}$$

The effects of collisions between particles is taken account of by the collision term denoted here by C_a. Here we attempt to describe the plasma in terms of its density

$$n = \int f(\vec{r},\vec{v},t)\, d\vec{v} \quad , \tag{3.4}$$

mean velocity

$$\vec{V} = \frac{1}{n} \int f(\vec{r},\vec{v},t)\vec{v}\, d\vec{v} \tag{3.5}$$

and certain higher velocity moments. For convenience, we have omitted the particle species subscript a. The first three moments of the kinetic equation yield conservation equations for particles, momentum and energy, as summarized below: [11]

Conservation of Particles

$$\frac{\partial n}{\partial t} + \nabla \cdot n\vec{V} = 0 \tag{3.6}$$

Conservation of Momentum

$$\frac{\partial}{\partial t} (mn\vec{V}) + \nabla \cdot mn\vec{V}\vec{V} + \nabla \cdot \vec{\vec{P}} - qn \left(\vec{E} + \frac{\vec{V} \times \vec{B}}{c} \right) = \vec{R} \tag{3.7}$$

where

$$\vec{R} = \int m\vec{v}\, C\, d\vec{V} \quad , \tag{3.8}$$

$$\vec{\vec{P}} = \int mf(\vec{v}'\vec{v}')d\vec{V} = p\vec{\vec{I}} + \vec{\vec{\pi}} \tag{3.9}$$

is the pressure tensor,

$$p = \frac{1}{3} nm \langle v'^2 \rangle \tag{3.10}$$

is the scalar pressure,

$$\vec{\vec{\pi}} = nm \left(\vec{V}\vec{V} - \frac{\langle v'^2 \rangle}{3} \vec{\vec{I}} \right) \tag{3.11}$$

is the stress tensor, and $\vec{v}' = \vec{v} - \vec{V}$ represents the deviation of particle velocity from the mean velocity.

Conservation of Energy

$$\frac{\partial}{\partial t} \left(\frac{nm}{2} \left(V^2 + \langle v'^2 \rangle \right) \right) + \nabla \cdot \vec{F} = qnE \cdot V + \vec{R} \cdot \vec{V} + Q \tag{3.12}$$

where

$$\vec{F} = \left[nm \left(\frac{V^2}{2} + \frac{\langle v'^2 \rangle}{2} \right) + p \right] \vec{V} + \vec{\vec{\pi}} \cdot \vec{V} + \vec{q} \tag{3.13}$$

is the total energy flux,

$$\vec{q} = nm \left\langle \frac{v'^2}{2} \right\rangle \vec{V} \tag{3.14}$$

is the heat flux, and

$$Q = \int \frac{mv'^2}{2} C \, d\vec{V} \tag{3.15}$$

So far, the equations are quite general and involve no assumption that the gas is collision dominated or retains a Maxwellian spectrum of velocities. Separate conservation equations may be written not only for different particle species, but also for different groups or particles of the same charge and mass. Primary electrons, for example, with significant

streaming energies could be treated as distinct from the main electron population which is taken to have a Maxwellian distribution of velocities. For the present, however, and until experimental or theoretical considerations dictate otherwise, we shall consider electrons as a whole and that their distribution varies slowly in space.

Approximation for Electron Gas

Consider that the plasma is in a steady state and that quasi-neutrality pertains throughout the bulk plasma (that is, away from electrodes and collecting surfaces). The electrons and ions each satisfy the particle continuity equation

$$\nabla \cdot n_i \vec{V}_i = 0 \qquad (i = +,-) \tag{3.16}$$

with $n_+ = n_- = n$. The momentum equation simplifies considerably if the electron drift velocity $\vec{V}$ is small compared to the random velocity $\langle v'^2 \rangle^{\frac{1}{2}}$ and if the velocity distribution is nearly isotropic. Then, in the absence of magnetic fields,

$$\nabla p + en\vec{E} = \vec{R}$$

where $\vec{R}$ represents the collisional drag between ions and electrons. In a classical plasma dominated by collisions, $\vec{R}$ is composed of a part proportional to the relative motion $\vec{u} = \vec{V}_e - \vec{V}_i$ between electrons and ions, leading to plasma resistivity, and to a thermal part proportional to the gradient of electron temperature, which is frequently neglected. In this approximation, Eq. (3.7) becomes

$$\nabla p + en\vec{E} = \eta\, ne\, \vec{j} \tag{3.17}$$

where $\vec{j}$ is the net current density and the plasma resistivity η is related to the electron-ion collision frequency ν_{ei} by

$$\eta^{-1} = \frac{\omega_p^2}{4\pi} \frac{1}{\nu_{ei}} \tag{3.18}$$

and ω_p is the electron plasma frequency. If the plasma is non-resistive and isothermal, Eq. (3.17) yields the barometric law, Eq. (3.1). In this sense, Eq. (3.17), or more generally the complete electron momentum equation, may be regarded as the generalization of the barometric law.

If the plasma is not collision dominated, randomization of electron velocities may still occur through the enhanced levels of fluctuating fields in the plasma, such as occur for electron two-stream instabilities, or electron-ion instabilities of the ion-acoustic or Bunemann type.[12,13] These mechanisms are probably effective in coupling neutralizer electrons into the bulk plasma and in equalizing electron and ion mean drift velocities. They are often approximated by introducing an effective collision frequency; e.g., in the case of the Bunemann mechanism, which is effective where the relative drift velocity between electrons and ions exceeds the mean thermal velocity of electrons

$$\nu_{eff}^{p} \sim \left(\frac{m_e}{m_i}\right)^{\frac{1}{3}} \omega_p ;$$

for scattering of electrons with velocity v from Langmuir oscillations with phase velocity v_p

$$\nu_{eff}^{p} \simeq \frac{\pi}{4} \omega_p \frac{v_p}{v} \frac{W^p}{nmv^2}$$

where W^p is the energy density in the wave. These expressions should be compared with the classical collision frequency

$$\nu = \frac{\pi}{4} \lambda_c \omega_p \frac{v_T}{v} \frac{W_T}{nmv^2}$$

where λ_c is the Coulomb logarithm, v_T, the electron thermal velocity and

$$\frac{W_T}{n} = \frac{\Theta}{n\lambda_D^3} \quad <<\Theta$$

is the fluctuation energy per particle in an equilibrium electron gas.

The determination of electron temperatures in the plasma requires consideration of the energy balance equation, Eq. (3.12). Making the same approximation in the equation expressing conservation of energy that were made in the momentum equation, yield

$$\nabla \cdot \vec{F} = qn\vec{E} \cdot \vec{V} + \vec{R}_e \cdot \vec{V}_e + Q_{ei} \tag{3.19}$$

with

$$F = \frac{5}{2} p\vec{V} + \vec{q} \tag{3.20}$$

Here 5/2 $p\vec{V}$ is the enthalpy flux of the drifting electrons, $\vec{q}$ the macroscopic heat flux, and $\vec{R} \cdot \vec{V}$ is related to the effective joule heating associated with the relative motion of electrons and ions. The quantity $\vec{R}$ appears also in the electron momentum equation; for a plasma controlled by collective effects it should be approximated in the energy equation in the same manner as in the momentum equation. The heat flux, $\vec{q}$, contains new features. Classically, $\vec{q}$, contains two terms; one proportional to the relative drift velocity between electrons and ions, and the other proportional to the gradient of electron temperature.[10]

For the initial calculations, the results of which will be reported later, we ignore the drift contributions to the energy flux, the electron-ion heating Q_{ei}, and assume that the heat flux is proportional to the temperature gradient. The energy balance equation thus assumes the simple form

$$\nabla \cdot K \nabla \Theta + mn\nu_{eff} \left(\bar{v}_e - \bar{V}_i\right)^2 = 0$$

3.2 ION ENGINE NEUTRALIZER CODE

The basic physics of an ion engine neutralizer model was presented in the preceding section. This physical model has been incorporated into a two-dimensional (R-Z) computer code, which is described below. Two sample calculations have been performed with this code: neutralization in a thruster similar to SERT II is discussed in Section 3.3., and a high resolution calculation of the temperature and density profiles near a hollow cathode neutralizer is presented in Section 3.4.

The ion thruster model has been incorporated into a two-dimensional (R-Z) computer code following the block diagram shown in Figure 3.1. For this initial version the ion currents and densities were assumed known. In a later version, it would be possible to allow a multicomponent ion composition to be determined self-consistently with the temperature and potential. The code operates entirely in MKS units.

The code has been run interactively, with all relevant information on disk file. As long as previous information exists on disk, the program may be entered from the two noted entry points as well as the beginning. For developmental

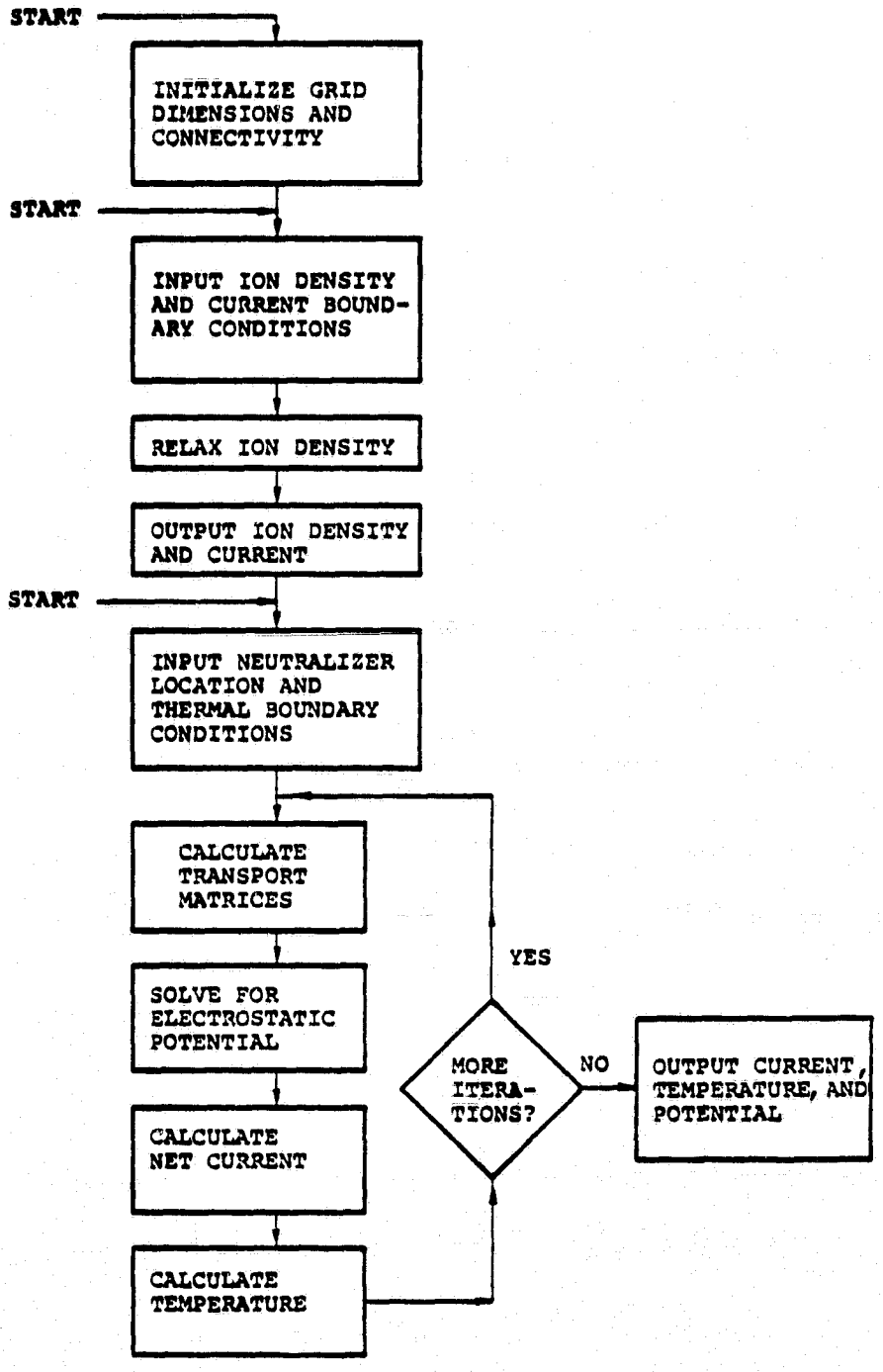

Figure 3.1. Block diagram for ion engine neutralization code.

purposes, it was found convenient to "hard-wire" many features of a particular problem into the code, while others are prompted for input. A flexible on-line graphics program, which plots information on the disk file, has also been developed.

At present, the code assumes ion velocities everywhere and ion currents at the input boundary to be known. The code then calculates plasma densities such that $\nabla\cdot(n\underset{\sim}{v}) = 0$ is numerically satisfied. Typically, ion velocities are taken to be either purely axial or to be radial from a point source on the axis exterior to the mesh. As the code requires non-zero plasma density everywhere, a background density of "slow" ions may be added. It should be possible to handle multiple ion species with interconversion fairly easily.

The neutralizer is assumed to be a ring at specified distance from the axis, emitting a current of electrons equal to the ion beam current. (In practice, this gives much too low a current density near the neutralizer. For this reason, we constructed a modified, high-resolution version of the code, focusing on the neutralizer to determine the temperature and potential profile near the neutralizer orifice.) The net current in the plasma is given by

$$\underset{\sim}{J}_{net} = ne\ (\underset{\sim}{\bar{v}}_{ion} - \underset{\sim}{\bar{v}}_{electron}) \tag{3.21}$$

$$= \sigma\ (-\nabla\phi + \frac{e}{n}\nabla p), \tag{3.22}$$

where σ is the plasma conductivity and $p = nkT$ is the electron pressure. [For $\sigma\to\infty$ and $ekT\to\theta$ (constant) we find $\phi = \theta \ell n\ n$.] The code determines electrostatic potentials by solving $\nabla\cdot\underset{\sim}{J}_{net} = 0$. (See Appendix B.) It is necessary to iterate between this equation and the temperature equation, since the pressure is a function of temperature.

The plasma temperature satisfies the equation

$$\underset{\sim}{\nabla}\cdot(-\kappa\nabla\theta) = \frac{J^2}{\sigma} \tag{3.23}$$

where κ is the thermal conductivity and the right-hand side represents the ohmic generation of heat. For this preliminary version, convective heat transport has been neglected. On the various boundary regions, either isothermal or insulating boundary conditions may be specified. In practice, since $\kappa = n\kappa'\theta^{n-1}$, the equation actually solved is

$$-\underset{\sim}{\nabla}\cdot\kappa'\underset{\sim}{\nabla}(\theta^n) = \frac{J^2}{\sigma} \tag{3.24}$$

For convenience, the transport coefficients σ and κ' are calculated by a single isolated subroutine. The conductivity σ may depend on both density and temperature, and κ' on density only. The present version assumes a relaxation rate proportional to the plasma frequency:

$$\sigma = n^{1/2}\,\frac{e^2}{m}\,\frac{1}{8.98\alpha} \tag{3.25}$$

where the parameter α is taken to be 0.51. By the classical Weideman-Franz law,

$$\kappa = \frac{3}{2}\,\sigma\,\left(\frac{k}{e}\right)^2\,T \tag{3.26}$$

If we measure temperature in eV, k = e, so that $\kappa' = \frac{3}{4}\,\sigma$.

3.3 BEAM NEUTRALIZATION CALCULATION

A calculation was performed for neutralization of a 0.25A, purely axial beam of 3 keV mercury ions in a constant density background plasma. The beam had a radius of ~ 7 cm, and a hot-wire ring neutralizer was placed at a 17-cm radius. These parameters were chosen to model the SERT II ion thruster. The plasma density (Figure 3.2) had a peak (central) density of 16.1×10^{14} m^{-3}, and an ambient density of 1.0×10^{14} m^{-3}. The electrostatic potentials are shown in Figures 3.3 and 3.4. The strong fields at the beam edge (Figure 3.3) are dominated by the barometric law, while the axial field at the beam entrance is needed to satisfy the boundary condition of stationary electrons and moving ions. Figure 3.4 (potentials at the thruster plane) shows the potential dip at the neutralizer position. The current-vector plots (Figures 3.5 and 3.6) indicate that the beam is neutralized by electrons entering from the side. The beam is 50 percent neutralized at ~ 15 cm downstream from the thruster. The temperature profile (Figure 3.7) was calculated with insulating boundary conditions at the thruster. The maximum temperature occurs at the beam entrance, where the heat generation is greatest. The peak temperature was 5 eV, compared with a 1 eV assumed background.

3.4 HIGH RESOLUTION CALCULATION OF TEMPERATURE AND DENSITY NEAR A HOLLOW CATHODE NEUTRALIZER

A version of the codes was constructed with .002 m radial resolution and .004 m axial resolution to treat the region in front of the "keeper" of a hollow cathode neutralizer. The parameters were chosen to approximate the plume mode experimental conditions of Siegfried and Wilbur[14] (Figures 3.8 and 3.9). A current of 2 ampere was assumed

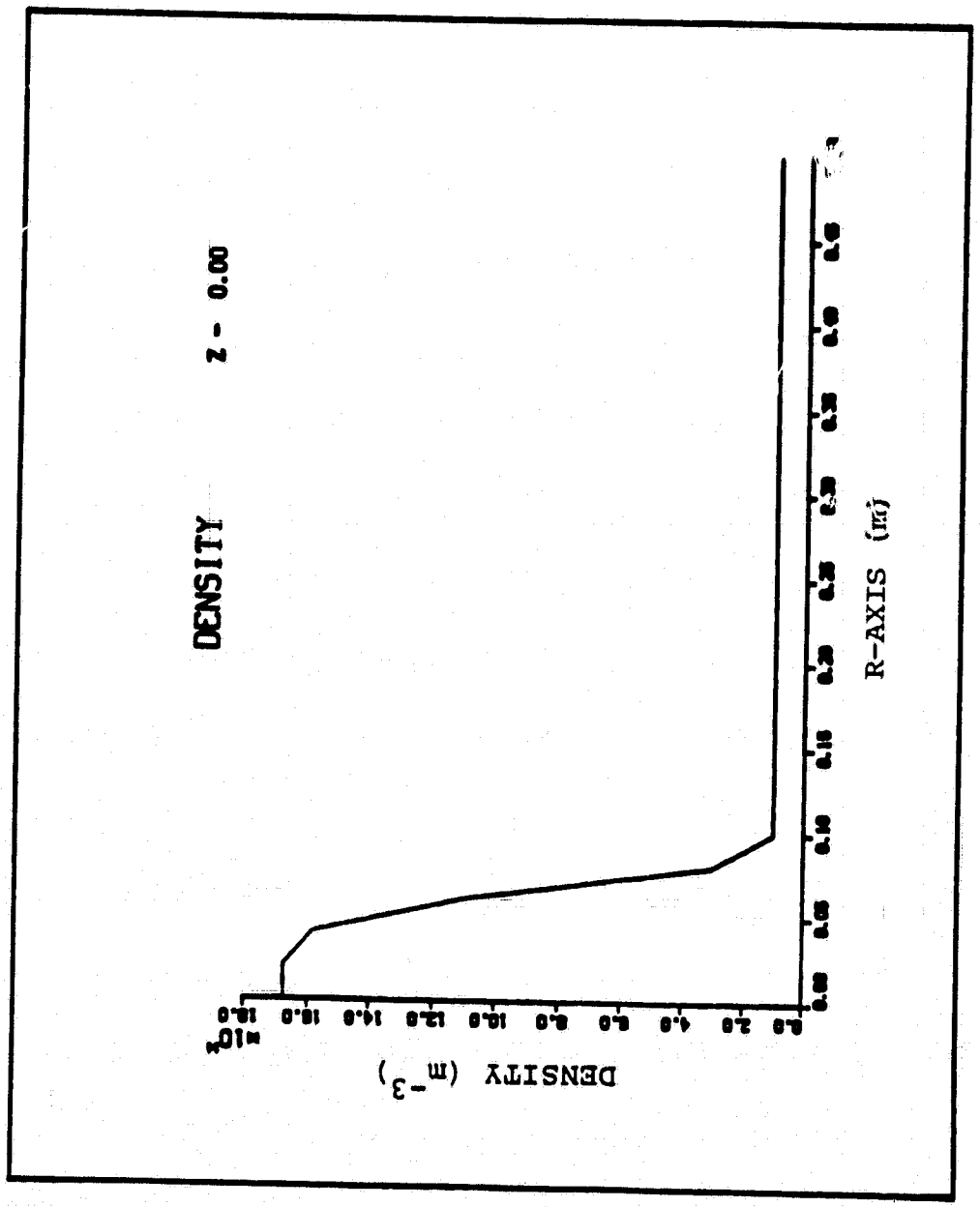

Figure 3.2. Plasma density for SERT II ion thruster model.

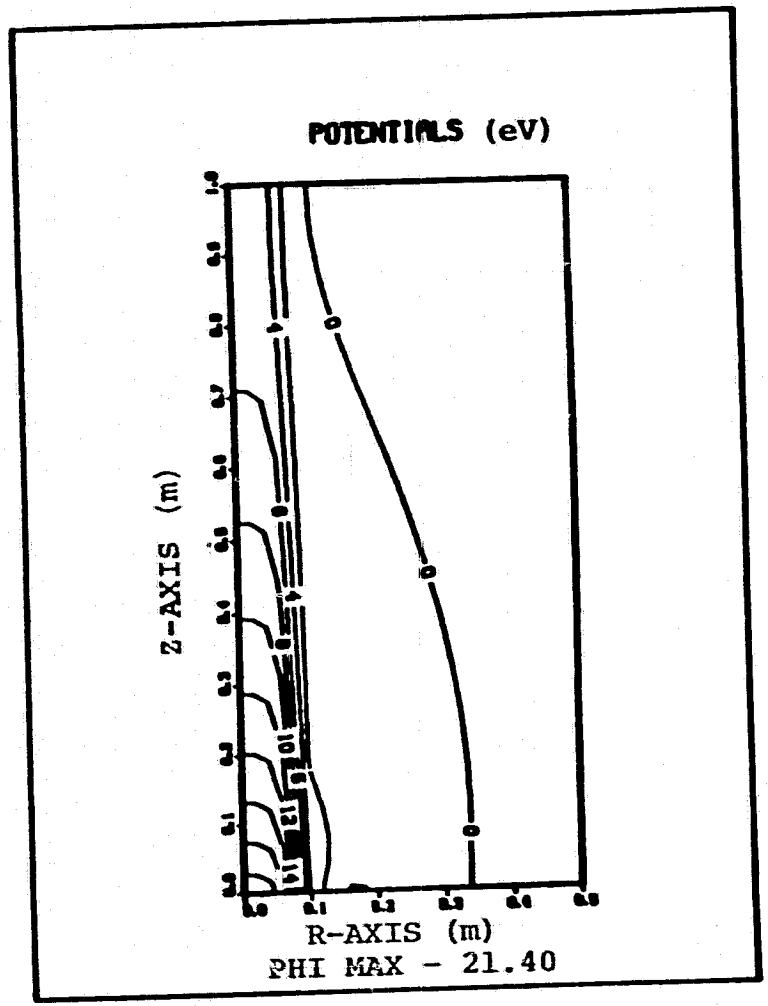

Figure 3.3. Electrostatic potentials for SERT II ion thruster model.

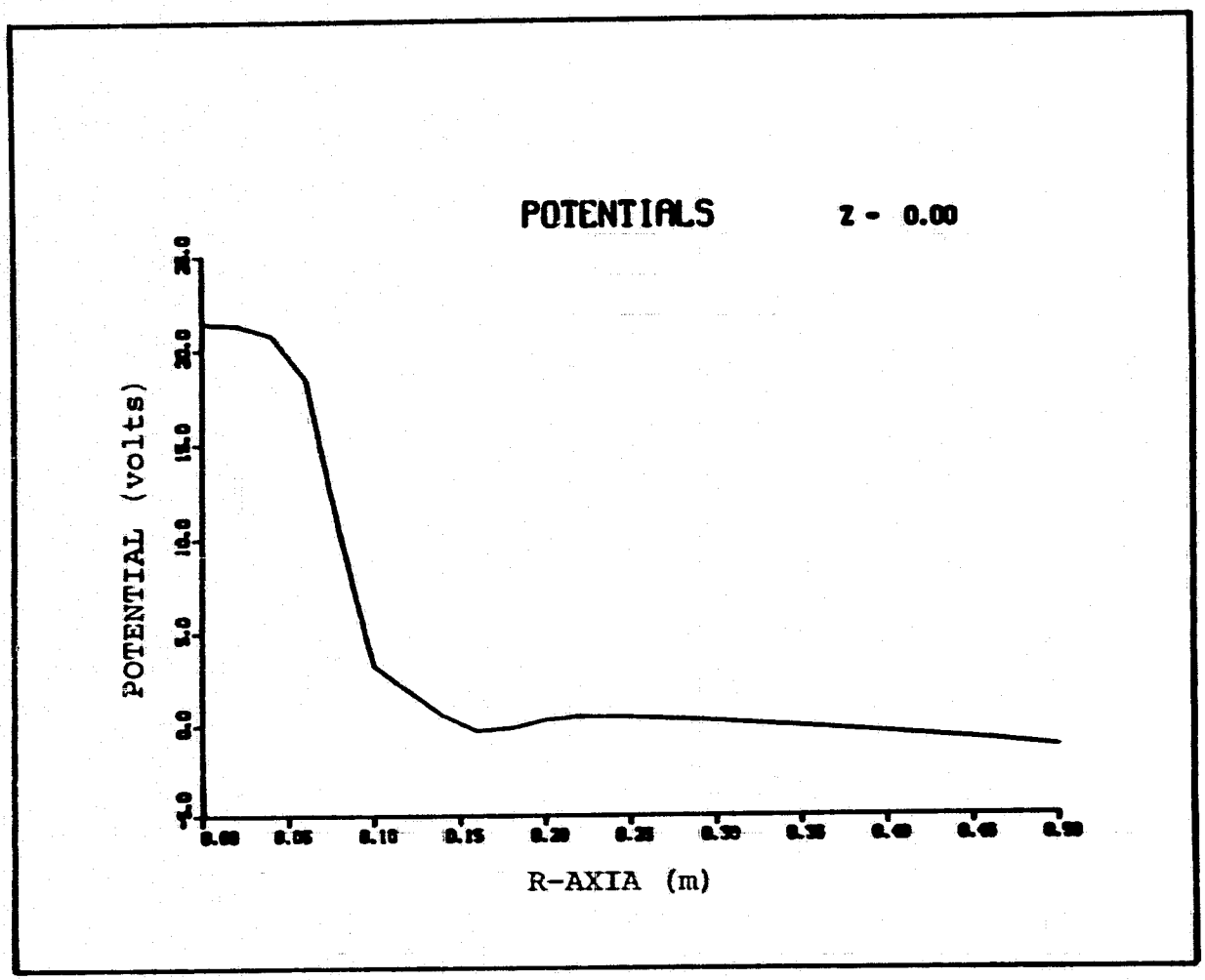

Figure 3.4. Electrostatic potentials for SERT II ion thruster model.

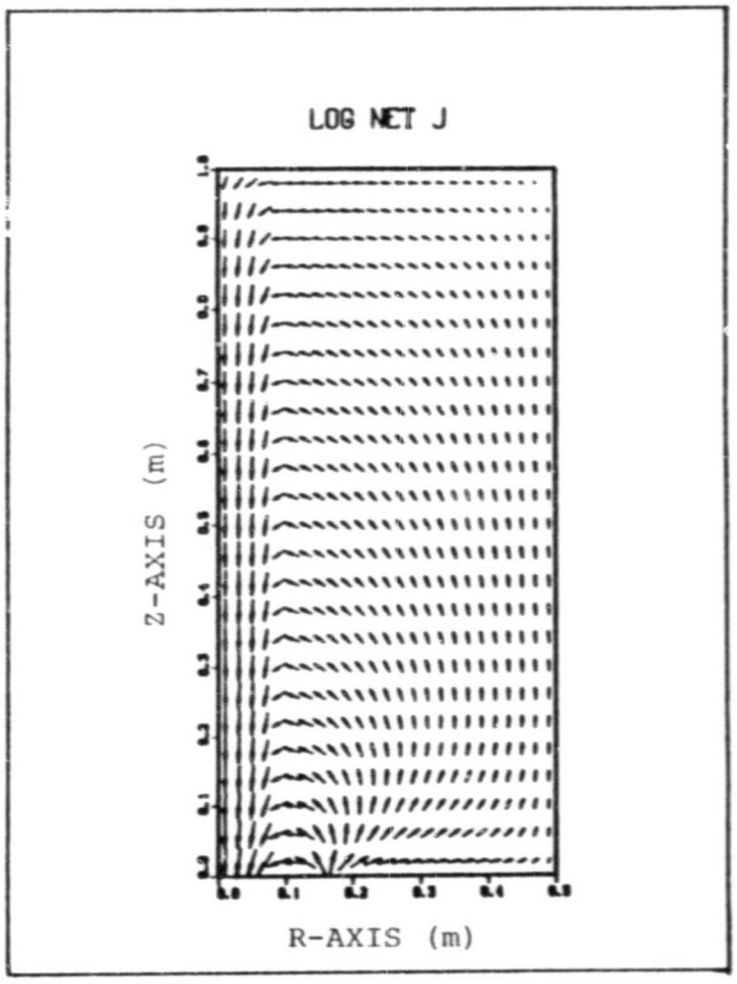

Figure 3.5. Current vectors for SERT II ion thruster model. The length of each arrow is weakly dependent on current.

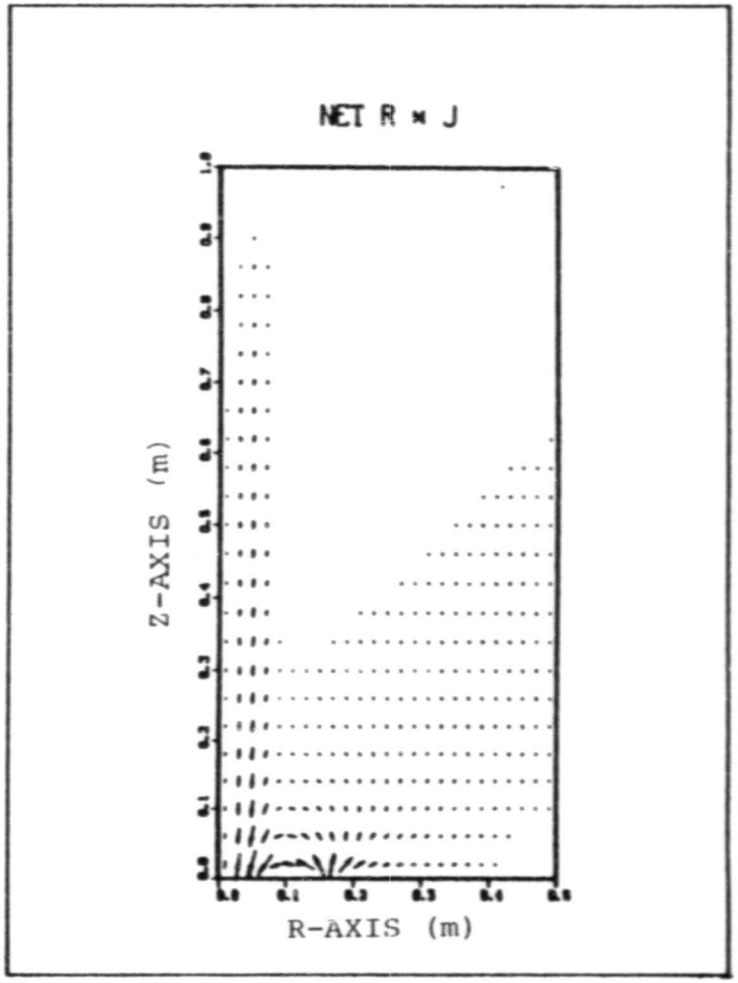

Figure 3.6. Current vectors for SERT II ion thruster model. The length of each arrow is proportional to radius times current density.

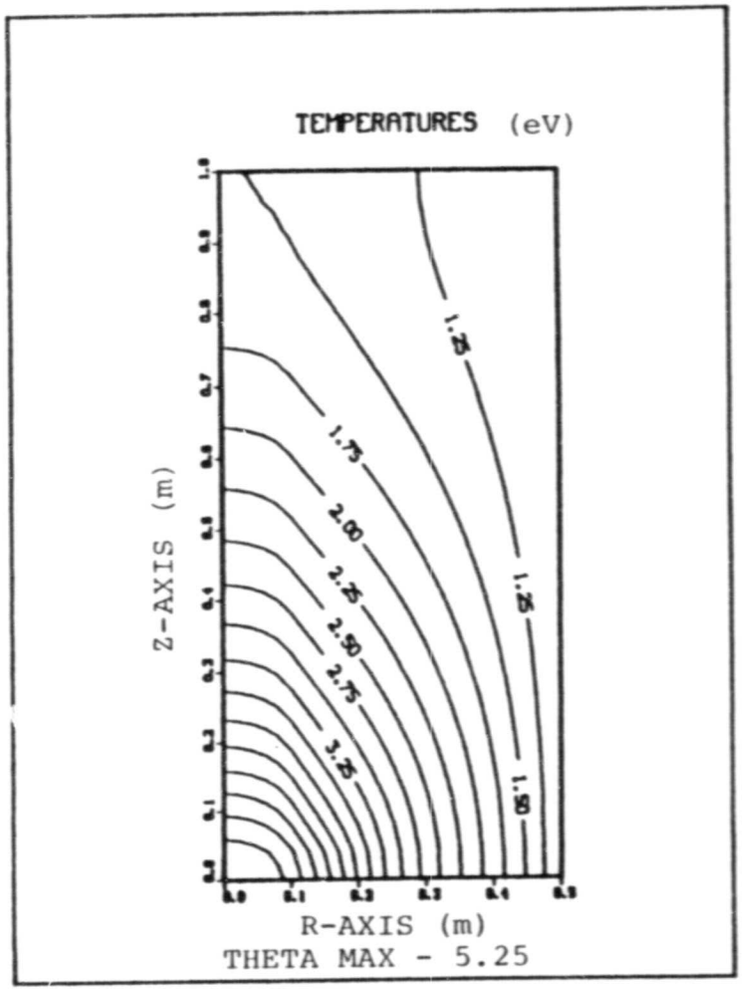

Figure 3.7. Temperature profile for SERT II ion thruster model.

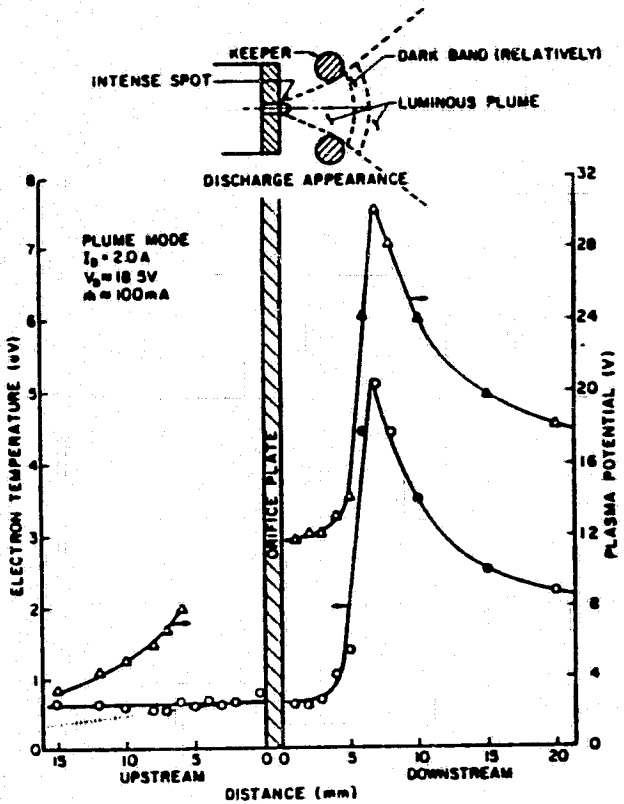

Figure 3.8. Cathode plasma potential and electron temperature profiles – plume mode (taken from Reference 14).

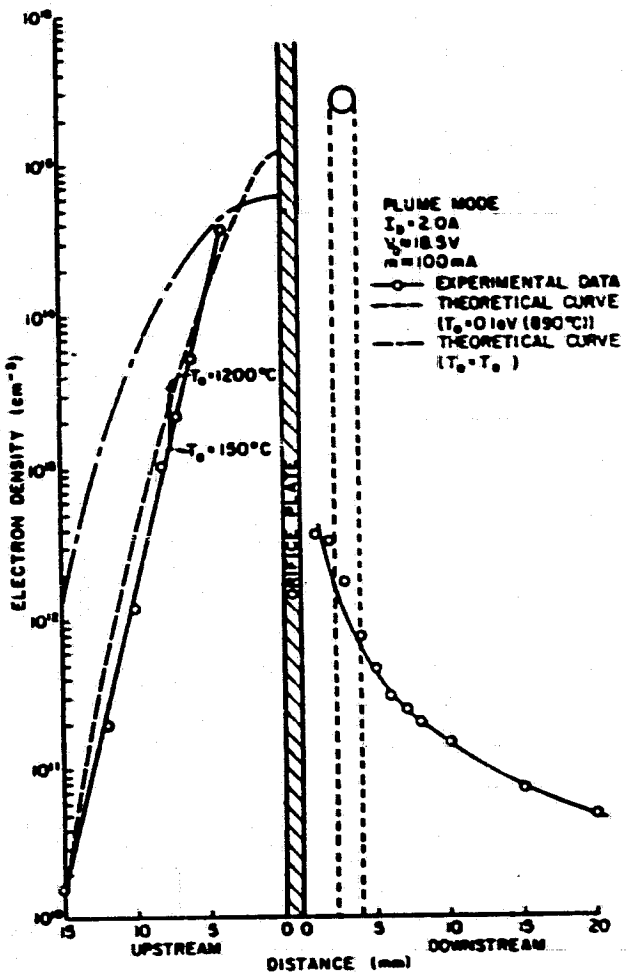

Figure 3.9. Cathode electron density profiles—plume mode (taken from Reference 14).

to flow through a 1 cm radius keeper. (Numerical difficulties, since resolved, prevented simulation of a 0.5 cm radius keeper.) Isothermal (1 eV) temperature boundary conditions were imposed at the keeper plane. The ions were assumed to flow radially from a source 1 cm behind the keeper, with a density of 10^{18} m^{-3} at the keeper (Figure 3.10). Our results (Figures 3.11 and 3.12) predict, in agreement with experiment, a sharp rise in both temperature and potential, followed by a gradual drop as one proceeds downstream from the keeper. The numerical agreement is quite good, and would probably improve considerably if the calculations were done with a smaller keeper. Substituting insulating thermal boundary conditions at the keeper plane (Figures 3.13 and 3.14) predicts far too much plasma heating.

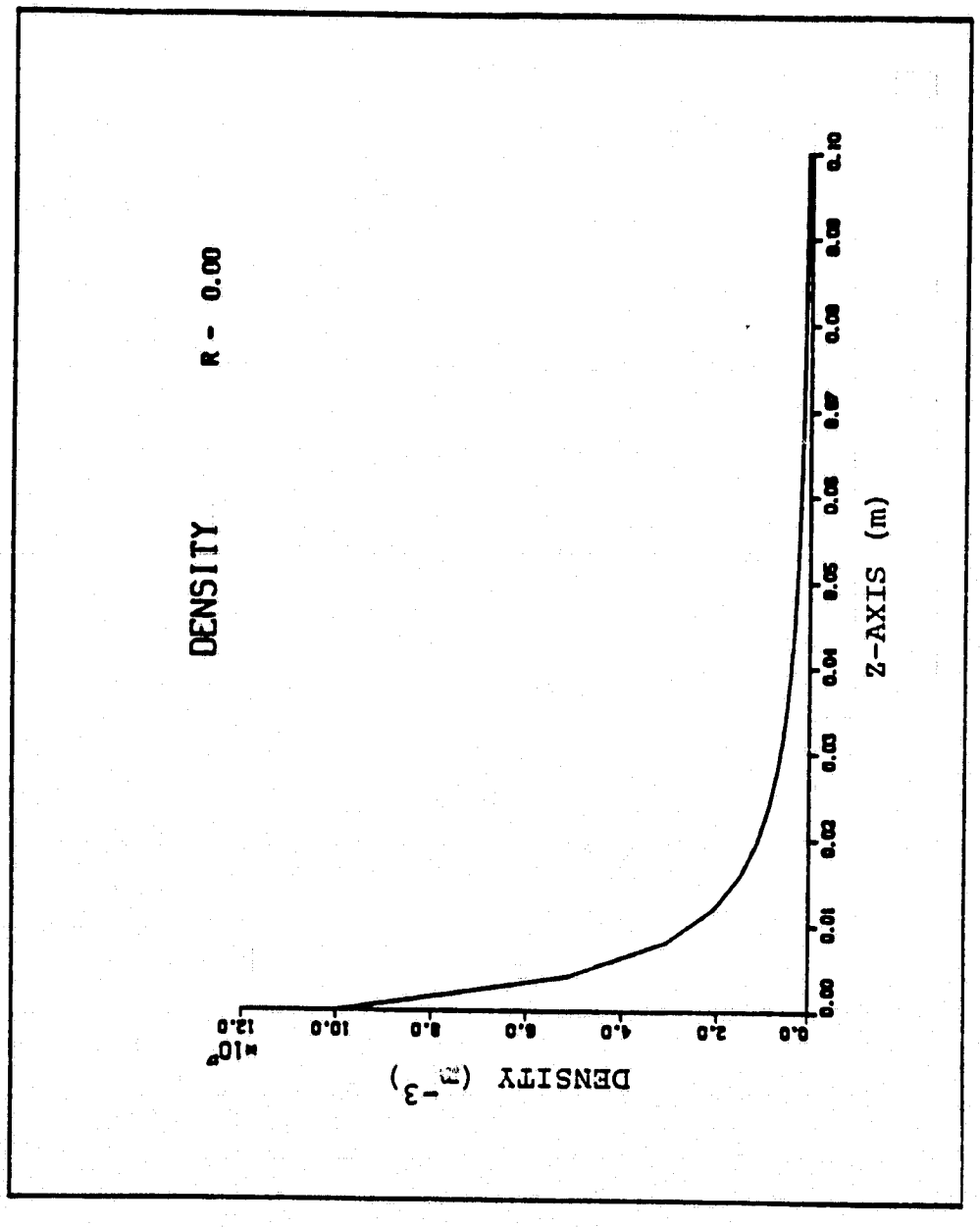

Figure 3.10. Ion density for hollow cathode neutralizer model.

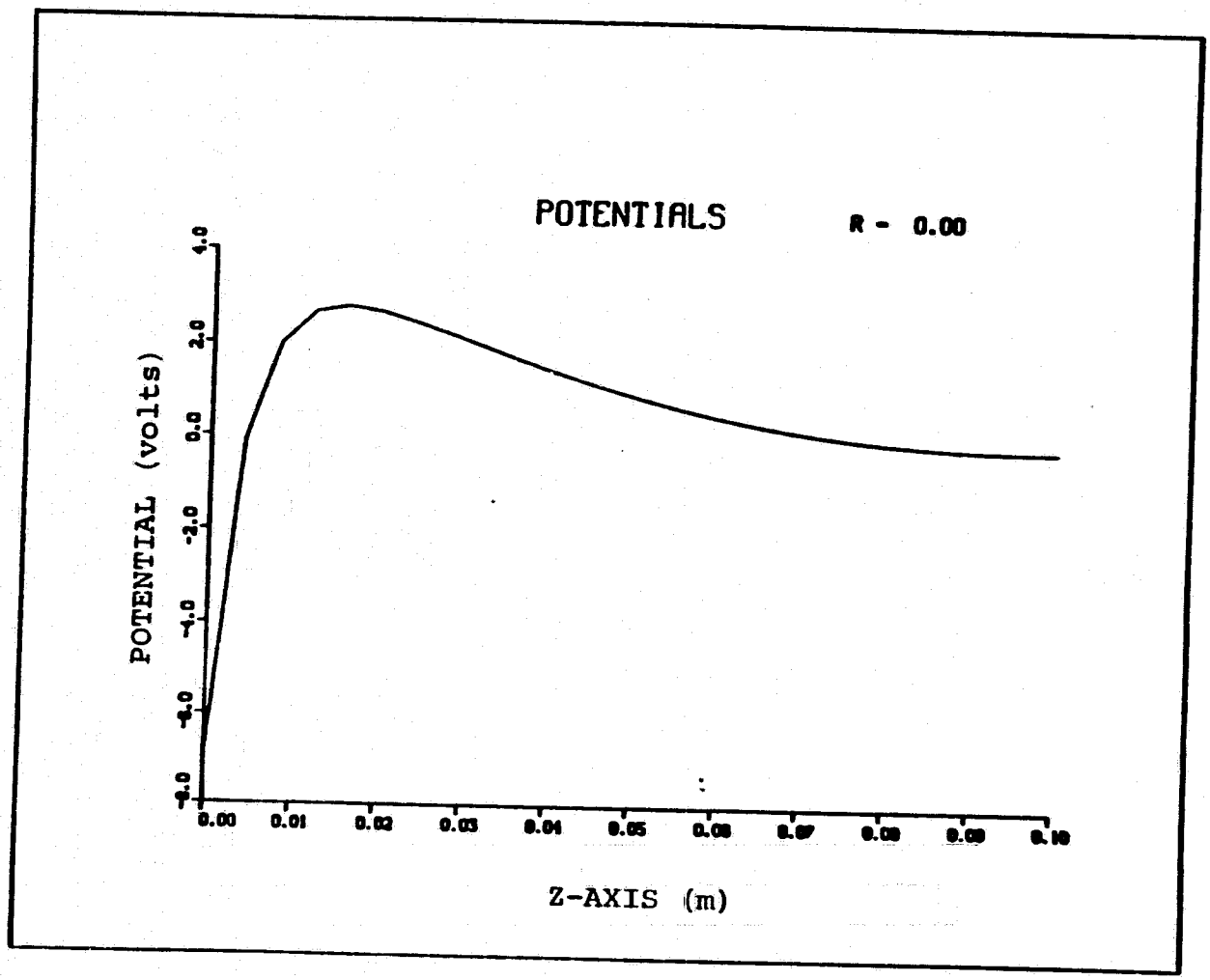

Figure 3.11. Electrostatic potentials for hollow cathode neutralizer model.

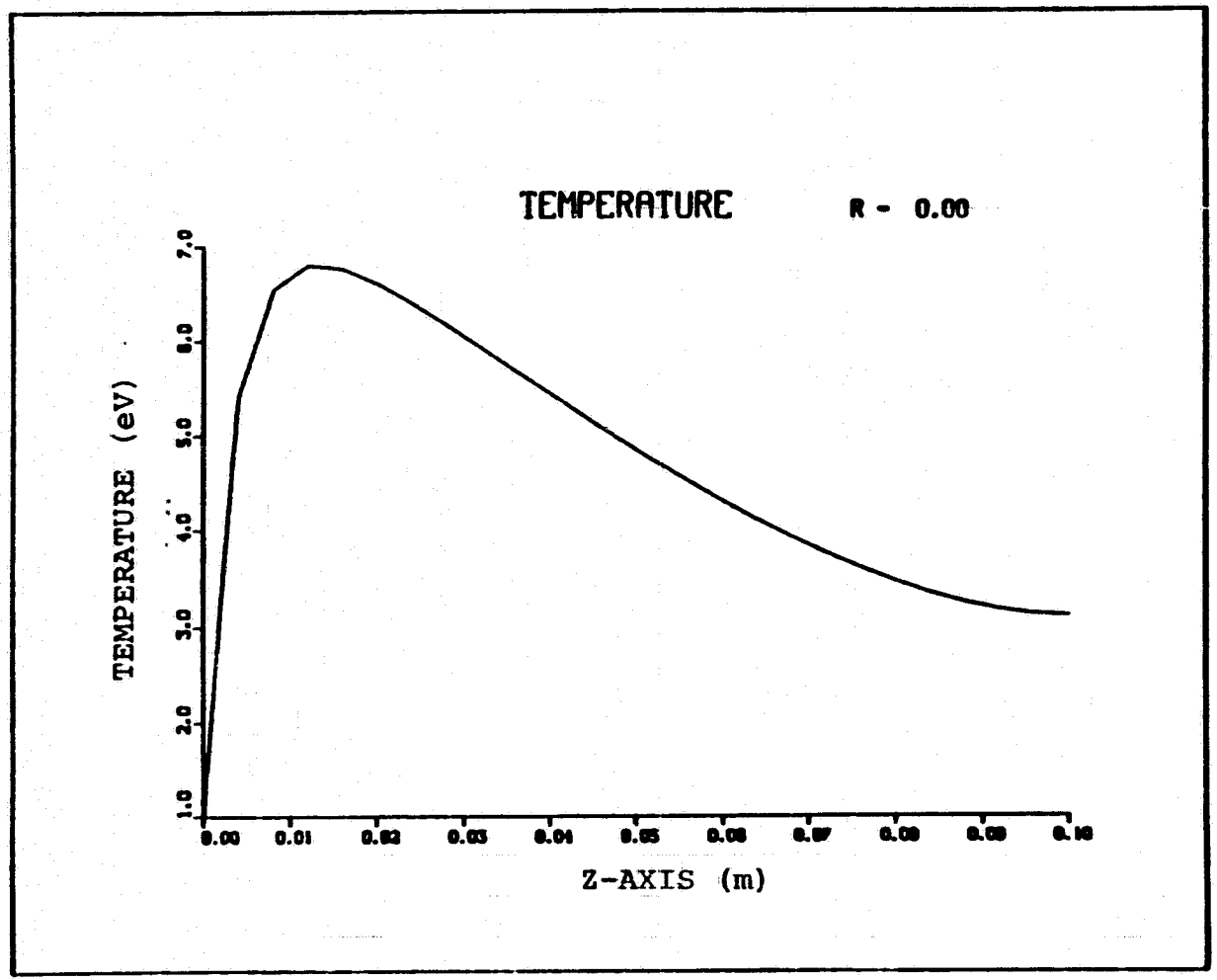

Figure 3.12. Electrostatic potentials for hollow cathode neutralizer model.

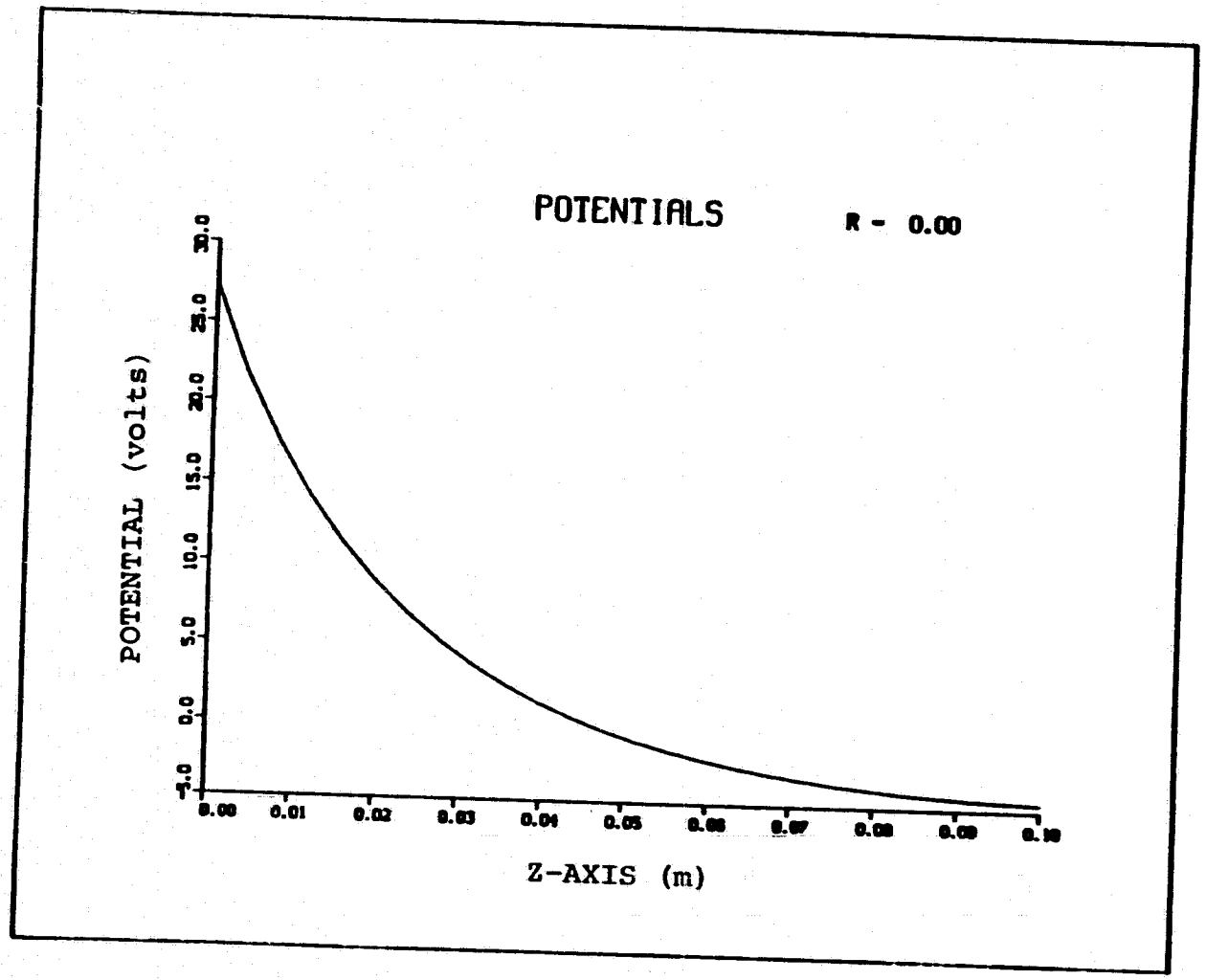

Figure 3.13. Electrostatic potentials for hollow cathode neutralizer, using insulating thermal boundary conditions.

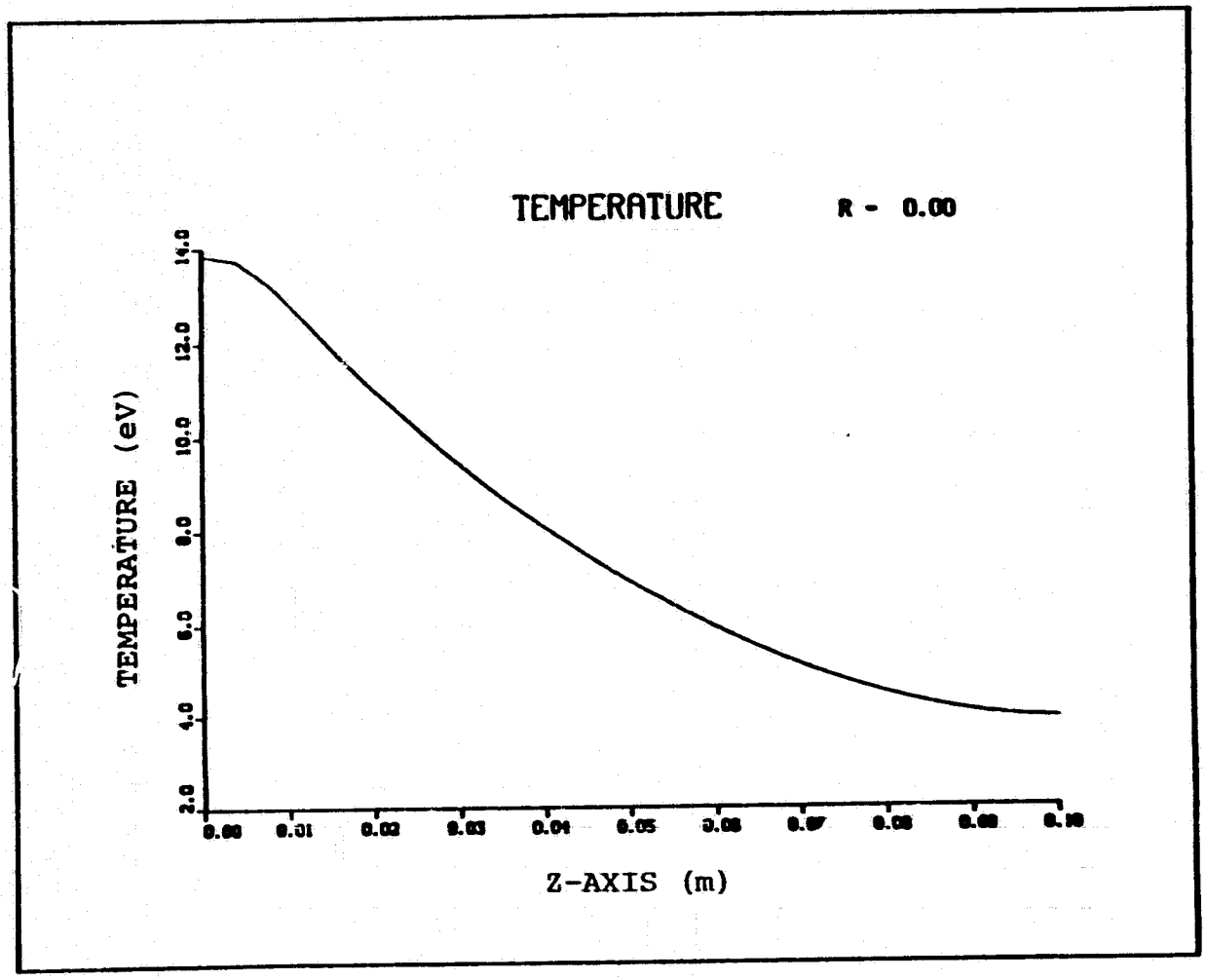

Figure 3.14. Temperature profile for hollow cathode neutralizer model, using insulating thermal boundary conditions.

4. ELECTROSTATIC ANTENNA MODEL

4.1 INTRODUCTION

The electrostatic antenna, or electrostatically controlled membrane mirror (ECCM), is one of several proposed systems (e.g., solar power satellites) involving the use of extremely high voltages in space. Laboratory and space experiments, as well as theoretical calculations, have indicated that interactions of such high voltages with the space environment can have severe adverse effects. For this reason, the Plasma Physics Group at Systems, Science and Software was asked to perform a study of this particular system with emphasis on identifying potential problems associated with spacecraft-environment interactions.

At present, specifications for an ECCM spacecraft are in the concept state. Its construction, orbit, and even its use are largely undetermined. The first systems study is not yet under way. The results of our investigation indicate that the ECCM is a viable concept in that we have found no potential problem that cannot be circumvented (or at least substantially alleviated) by careful design. However, sputtering in LEO is of uncertain magnitude and warrants further consideration. We feel that the information presented herein should be important input to any future systems or design studies.

In Section 4.2, we summarize the basic concept of the ECCM, with particular emphasis on how various design features relate to spacecraft-environment interactions. Section 4.3 describes the plasma environment in low-earth and geosynchronous orbit. Section 4.4 discusses spacecraft charging: the effects it may have on the membrane shape, as well as the possibility of actual damage. Section 4.5 discusses parasitic power losses involved in maintaining the high voltage. Section 4.6 evaluates possible sputtering damage to the

large areas of the membranes and coatings. We present our conclusions in Section 4.7.

4.2 DESIGN SUMMARY

The ECCM concept has been described elsewhere by Mihora and Redmond.[15] The basic strategy is to use electrostatic pressure

$$\underset{\sim}{t}_e = \varepsilon_o \left[(\underset{\sim}{E}\cdot\hat{n})\ \underset{\sim}{E} - E^2\hat{n}/2 \right]$$

to form and (through electronic feedback) finely adjust the shape of a conductively-coated membrane. The nominal operating conditions are a 50 kV potential across a 10 cm gap, thus giving a pressure of $\sim$1 nt/m^2, which is five orders of magnitude smaller than atmospheric pressure, but five orders larger than solar radiation pressure. The baseline system is a 100 m diameter antenna with positively biased, concentric ring electrodes.

For future reference we set down here, in simplest form, some relations between membrane tension, shape, and applied pressure. The vector diagram below indicates the forces on a small circular piece of membrane. The electrostatic force, $\pi r^2 \underset{\sim}{t}_e \cdot \hat{n}$, is opposed by the upward component of the membrane tension t_m (Figure 4.1). Thus, if the radius

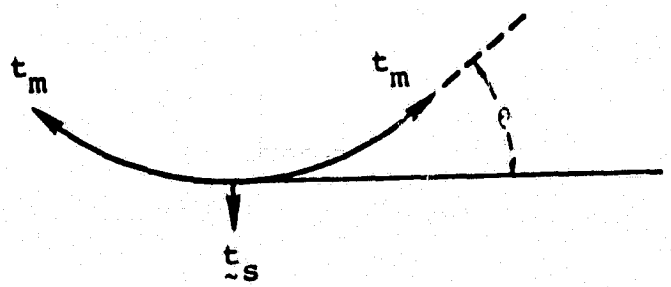

Figure 4.1. Force balance vector diagram for a small section of membrane.

of curvature of the membrane is R_c, we have

$$\pi r^2 \, \underset{\sim}{t}_e \cdot \hat{n} = 2\pi r t_m \sin\theta \approx 2\pi r t_m \frac{r}{R_c}$$

$$t_m = \frac{R_c}{2} (\underset{\sim}{t}_e \cdot \hat{n}) \quad .$$

For the system under consideration, $\underset{\sim}{t}_e \cdot \hat{n} \approx 2 Nt/m^2$, $R_c \sim 100$ m, so the membrane tension is $t_m \approx 100$ nt/m.

Some drawings of possible ECCM designs are shown in Figures 4.2 and 4.3. All have the same basic features:

- The high-field region is bounded by the membrane above, the electrode below, and some circumferential mounting structure.
- The region behind the high-voltage electrode contains dielectric support structures. There may be substantial electric field in this region as well. The rear of the structure is also covered with membrane material.
- An electronics package above the center of the antenna is held by booms mounted on the circumferential mounting structure.
- Solar panels and other spacecraft hardware are mounted behind the antenna structure.

The emphasis of this analysis is on the high-field region and on the membrane separating it from the plasma environment. Also of primary importance is the amount of plasma leakage near the membrane circumference.

The candidate membrane materials are 0.0005 inch (13 μm) mylar with both sides aluminized to 1 Ω/□ surface resistivity (about 350 A of aluminum); 0.0003 inch (8 μm) Kapton (presently available with one side aluminized); and various forms of metallized cloth. The material thicknesses

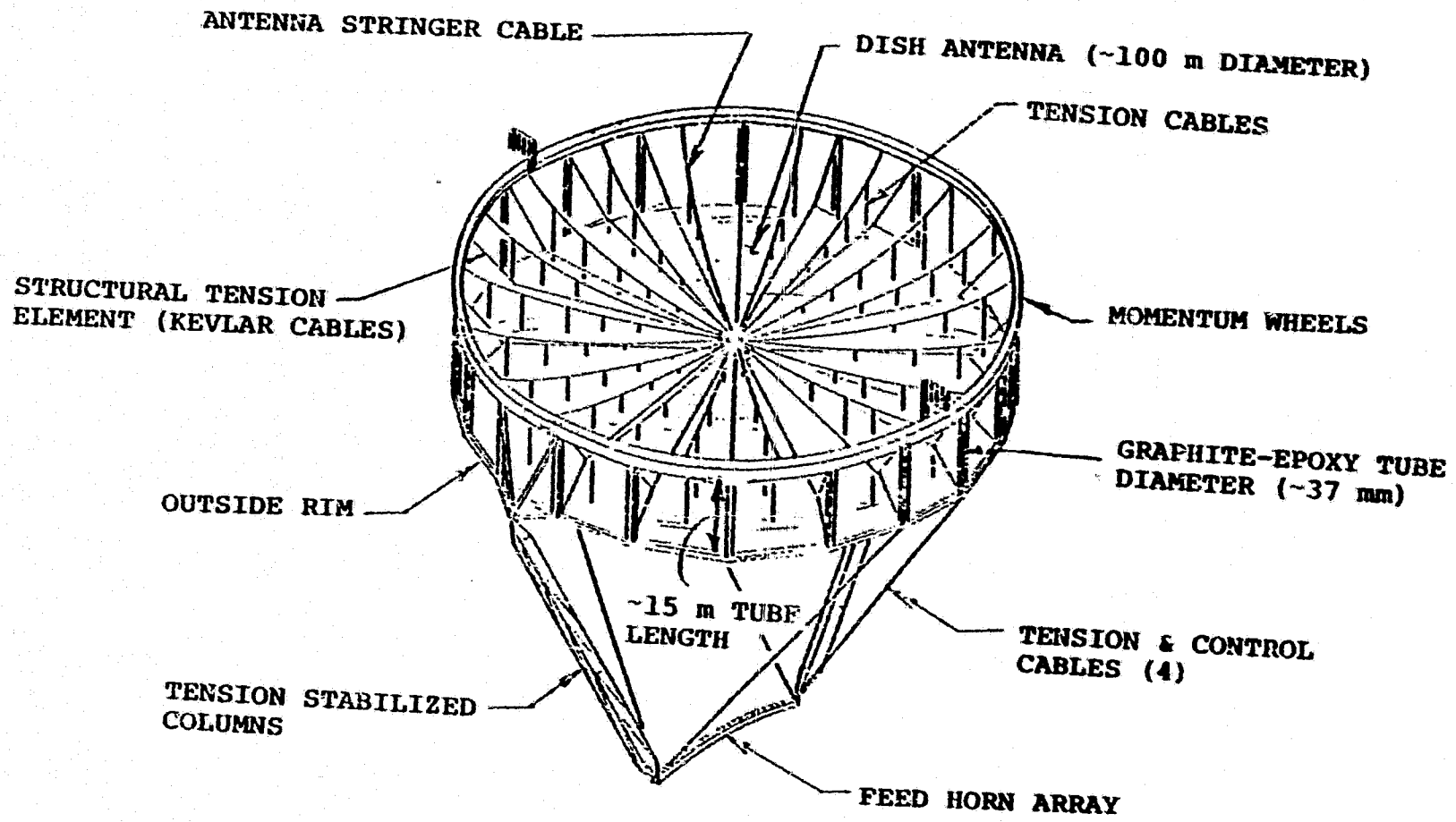

Figure 4.2. Hoop tension configuration for ECCM.

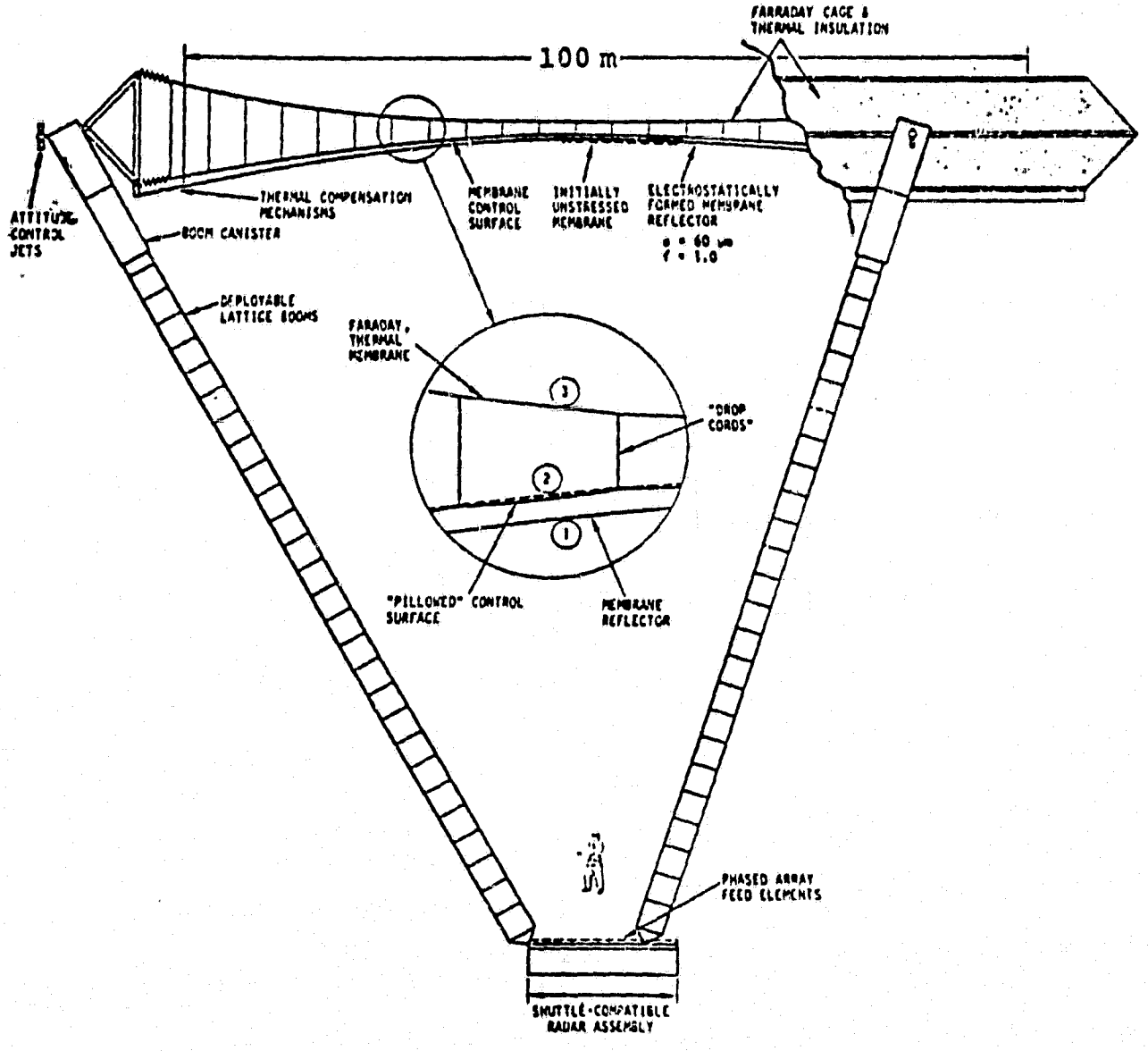

Figure 4.3. Three-membrane truss design for ECCM.

are such as to respond to the low values of pressure provided by the electric field without being excessively difficult to handle.

Systems designers must take into consideration the thermal control aspects of having a large area of doubly aluminized membrane. While from an electrical point of view such material has great advantage in ensuring against loss of metallization, possible thermal problems may well need to take precedence.

4.3 ENVIRONMENT SUMMARY

We were asked to consider interactions of the electrostatic antenna with the space environment in both low-earth orbit (LEO, ∿200 km altitude) and geosynchronous orbit (GEO, ∿7 R_e altitude). We did not consider the possibility of polar orbit. While the ambient plasma in space is very tenuous, it is not negligible. Even in GEO, where the density is about 1 cm^{-3}, environment interactions have caused spacecraft malfunctions and even permanent damage. In low-earth orbit the plasma is colder and denser (10^4-10^6 cm^{-3}) and has even greater potential for causing problems to high-voltage systems.

In Tables 4.1 and 4.2 we indicate the range of parameters characterizing the low-earth and geosynchronous environments. While the SCATHA spacecraft is returning additional data on the GEO plasma, it is already clear that this environment is extremely variable and any design must take its full range into account. In interpreting Table 4.1, it should also be kept in mind that characterizing the plasma by a temperature tends to underestimate the high energy portion of the spectrum. For a thorough review, see Reference 16.

Table 4.1. Geosynchronous Plasma Environment

	Low	Typical	High
Plasma Density	10^5 m^{-3}	10^6 m^{-3}	5×10^6 m^{-3}
Electron Temperature	<1 keV	1 keV	10 keV
Ion Temperature	1 keV	5 keV	20 keV
Electron Current	10^{-7} A/m^2	10^{-6} A/m^2	3×10^{-6} A/m^2
Ion Current	10^{-8} A/m^2	3×10^{-8} A/m^2	10^{-7} A/m^2
Debye Length	1 m		10^3 m

Figures exclude particles with ε < 50 eV.

Table 4.2. Low-Earth Orbit Environment

Plasma Density	10^{10} - 10^{12} m^{-3}
Neutral Density	~ 10^{16} m^{-3}
Plasma Temperature	~ 0.1 eV
Debye Length	~ 1 cm
Spacecraft Velocity	7500 m/sec
Ram Ion Current	~ 10^{-3} A/m^2
Ram Ion Energy	~ 5 eV

The LEO (up to 1000 km) plasma has been studied for many years by electromagnetic, rocket and satellite probes. A thorough summary is available in Reference 17. The plasma density has a maximum of 10^5-10^6 cm^{-3} in the range of 300 to 400 km. It drops off sharply below 250 km. Above 500 km, it varies slowly with altitude, maintaining a value of 10^4-10^5 cm^{-3}. The plasma temperature takes a value of $\sim$0.1 eV from 200 to 500 km, though some measurements are as high as 0.3 eV. Below 200 km, the temperature decreases to $\sim$0.05 eV at 100 km.

An additional feature in LEO is the presence of ram ions. Since the spacecraft velocity ($\sim$7.5 km/sec) exceeds the ion velocity ($\sim$1 km/sec), the forward side of the spacecraft is constantly bombarded with $\sim$5 eV ions and neutrals, which may, in some instances, cause sputtering problems.

Photoemission due to sunlight is another environmental factor to be considered in both LEO and GEO. Most materials photoemit $\sim 2\times10^{-5}$ A/m^2 of low energy ($\sim$2 eV) electrons when exposed to solar ultraviolet radiation. Photocurrent is particularly important in GEO, where it is usually more than sufficient to maintain the spacecraft at positive potential. The excess photoelectrons then form a sheath of relatively dense plasma around the spacecraft, capable of supporting fairly considerable parasitic currents.

In LEO, however, the photocurrent is considerably smaller than the electron thermal current and comparable to the ion (thermal or ram) current. Thus, the spacecraft will normally remain at a slight negative potential in sunlight, and no photoelectron sheath will form. However, when a spacecraft has applied differential potentials, photoemission should still be considered as a possible source of parasitic current.

4.4 EFFECTS OF SPACECRAFT CHARGING

Spacecraft charging is an effect which occurs fairly frequently at geosynchronous altitude when a satellite encounters a "geomagnetic substorm". During such events, a very hot ($\sim$10 keV) plasma can cause uniform (negative, relative to plasma ground) or differential potentials comparable to the plasma temperature. The differential potentials can lead to arcing, causing malfunctions by, or damage to, spacecraft.

To prevent differential charging, the ECCM is designed to be conducting over its entire surface. This is accomplished by covering the antenna structure with membrane material, which we will assume to be aluminized plastic. Thus, in analyzing spacecraft charging effects, we must concentrate on what flaws are likely to develop in this scheme and what effects these may have on the antenna performance.

The type of charging not eliminated by the "Faraday cage" structure is overall (uniform) charging. If the antenna charges uniformly to -10 kV, one would expect fields $\sim 10^2$ V/m near the antenna center and $\sim 10^4$ V/m near its periphery. These fields will create small electrostatic pressures ($< 10^{-3}$ nt/m^2) opposing the applied pressure ($\sim$1 nt/m^2). With the proposed feedback system, these stray pressures will be automatically compensated for by imperceptible ($\lesssim$0.1 percent) changes in the electrode voltages.

Differential charging within the membrane due to buildup of trapped charge remains a possibility. If we consider a doubly aluminized plastic membrane of thickness 10^{-5} m, incident electrons with energies in the range of 1 keV $\lesssim \varepsilon \lesssim$ 20 keV will be trapped. If the current of such electrons is 10^{-5} A/m^2, internal potentials will build up

at the rate of a few volts/sec, or internal electric fields at a few times 10^5 volts/cm-sec. Since the intrinsic conductivity can be 10^{-18} mho/m or less, electric fields of 10^8 V/m may be required to balance the incident current. Such fields are in excess of the material's dielectric strength. High-field and radiation-induced conductivity will serve to reduce the likelihood of achieving breakdown potentials, but the possibility of occasional small arcs within the membrane must be acknowledged. These arcs will cause some material damage and some loss of metallization. Most likely, however, these effects will be sufficiently rare and sufficiently localized that they will not be significant.

Granting the possibility of some loss of metallization, we may address the question of how big a damage spot will degrade the antenna performance. A damage spot will have a substantial pressure reduction, and a displacement given by the square of the spot dimension divided by the radius of curvature:

$$\delta \approx x^2/R_c \quad .$$

Thus, a 10^{-4} m displacement in an antenna with 100 m radius of curvature will result from a 10 cm damage spot. We believe development of such a large spot to be rather unlikely.

Another easily avoided charging problem is differential charging of booms. Normal graphite-epoxy booms are sufficiently conductive to avoid charge buildup (required is surface resistivity less than 10^8 $\Omega/\square$) while being resistive enough not to interfere with antenna function. Care must be taken, however, to avoid isolating a boom through use of insulating spacers or mountings.

4.5 PARASITIC POWER LOSS

An important neglected area that was not addressed in the preliminary design of the ECCM is the question of power loss. Any plasma entering the high-field region of the antenna constitutes a parasitic current and, when multiplied by the applied voltage, a power loss. We have had little input as to what would be an acceptable power loss. Consequently, in this section we adopt the point of view that a kilowatt power loss is unacceptable, a one hundred watt power loss is a significant design consideration, and a power loss of ten watts or less is acceptable.

There are three main avenues through which plasma (i.e., electrons) can enter the high-field region:

- Through holes or gaps in the "Faraday cage." We anticipate such gaps at the circumference of the membrane, where it is attached to the structure.
- If metallized cloth is used, stray fields penetrating the weave will enhance plasma collection through the membrane.
- If a thin plastic membrane is used, high energy electrons will penetrate through the membrane into the electrode region.

We consider the latter two mechanisms in some detail below. First, however, we discuss the magnitude of current provided by the spacecraft environment.

4.5.1 Environmental Sources of Current

The first-order estimate of environmental current is the one-sided plasma thermal current:

$$J_o = n_o\, e(k\theta/2\pi m)^{1/2} \quad .$$

Values for several environments are given in Table 4.3. Of these, the first three (low-density) cases represent quiet, moderate, and fairly severe geosynchronous conditions, while the two higher density cases bracket the LEO environment. Also shown is the typical photoemission current due to solar ultraviolet.

In Table 4.4 these current densities are multiplied by 50 kV to yield a power loss. The values in the electron (e^-) column may be taken as reasonable upper bounds. From these figures, it is apparent that in LEO even 1 m^2 total opening in a membrane of 10^4 m^2 area is likely to produce an intolerable power loss. In GEO, however, a few square meters of opening may well be tolerable, provided enhanced collection of photoelectrons by stray fields is not too severe. (See Appendix C.)

Another possibility suggested by these tables is to bias the electrode negative. The ion currents which may be collected are far lower than the electron currents, and leakage of negative field would not lead to photoelectron collection. In GEO, this would allow a great deal of latitude for openings and gaps in the membrane. It is unlikely that collected ions would cause sputtering problems. While negative bias may also be useful in LEO, the possibility of sputter damage for long-term missions must be considered.

4.5.2 Field and Plasma Penetration Through Cloth Weave

It has been suggested that metallized cloth be considered as an alternative to aluminized plastic for use as membrane material. Metallized cloth has been flown successfully in the past; for example, the ATS-5 antenna was made of 70 percent transparent copper-clad Dacron. Suitability

Table 4.3. Plasma Thermal Current
$J_o = n_o\, e[k\theta/2\pi m]^{\frac{1}{2}}$ (A/m^2)

n_o	Θ	e^-	H^+	N_2^+	
1 cm^{-3}	1 eV	2.7×10^{-8}	6.3×10^{-10}	1.2×10^{-10}	
1 cm^{-3}	1 KeV	8.5×10^{-7}	2.0×10^{-8}	3.8×10^{-9}	
1 cm^{-3}	10 KeV	2.7×10^{-6}	6.3×10^{-8}	1.2×10^{-8}	
10^4 cm^{-3}	1 eV	2.7×10^{-4}	6.3×10^{-6}	4×10^{-6}	(ram)
10^6 cm^{-3}	1 eV	2.7×10^{-2}	6.3×10^{-4}	4×10^{-4}	(ram)
(SUNLIGHT)		3×10^{-5}			

Table 4.4. Power Loss (W/m^2)
@ 50 KV

n_o	Θ	e^-	H^+	N_2^+
1 cm^{-1}	1 eV	1.3×10^{-3}	3.1×10^{-5}	6×10^{-6}
1 cm^{-3}	1 KeV	4.3×10^{-2}	1.0×10^{-3}	1.9×10^{-4}
1 cm^{-3}	10 KeV	0.13	3.1×10^{-3}	6×10^{-4}
10^4 cm^{-3}	1 eV	13	0.31	0.2
10^6 cm^{-3}	1 eV	1300	31	20
(SUNLIGHT)		~1		

for rf applications does not, however, imply adequate blockage of very high dc fields or impinging electrons. For this reason, we used a modified version of the fine resolution LEO current collection code to study field penetration and leakage of low-energy plasma through such material.

Representation of two different grades of cloth material is illustrated in Figure 4.4. (The illustrated structures are periodically contained so as to make a full membrane.) The two cloths have square cross-section fibers, with spacing-to-diameter ratios of 8:1 and 4:1, giving nominal transparencies of 77 percent and 56 percent. We first calculated the potential (Figure 4.5) above and below the cloth in a configuration of high electric field below the grounded membrane, and a ground plane (possibly representing a sheath edge) several fiber diameters above. We found the field above the coarser membrane ∿4 percent of that below, and correspondingly 1 percent for the finer cloth. From this we may expect the mean potential of a cloth membrane to be ∿1 percent of the high voltage electrode, i.e., ∿500 volts.

We then proceeded to calculate the apparent transparency of the membrane for low-energy electrons emitted from the ground plane. As seen in the particle trajectories, Figure 4.6, a substantial amount of focusing took place. In both cases the penetration exceeded the nominal transparency by about 20 percent. These results are summarized in Table 4.5.

These calculations lead to the conclusion that a substantial fraction of electrons incident on a metallized cloth membrane will appear as parasitic current. Thus, there will be an intolerable power drain of several kilowatts due to photoelectrons alone. We are forced to conclude that metallized fabric is not suitable for use in the ECCM.

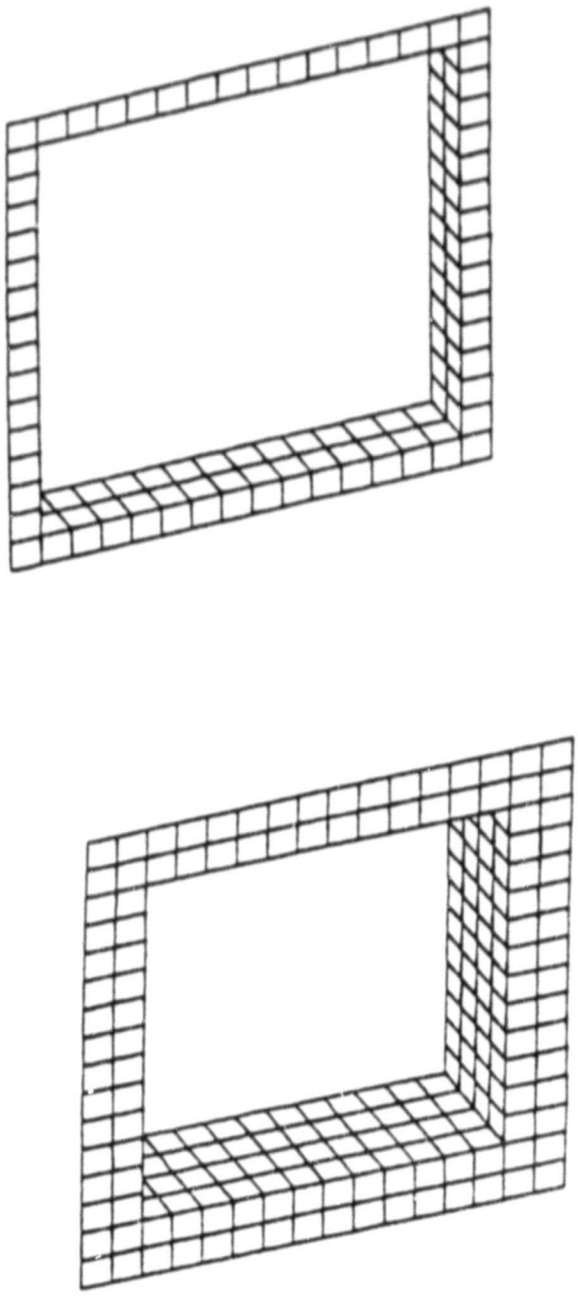

Figure 4.4. NASCAP representations of hole in metallized cloth.

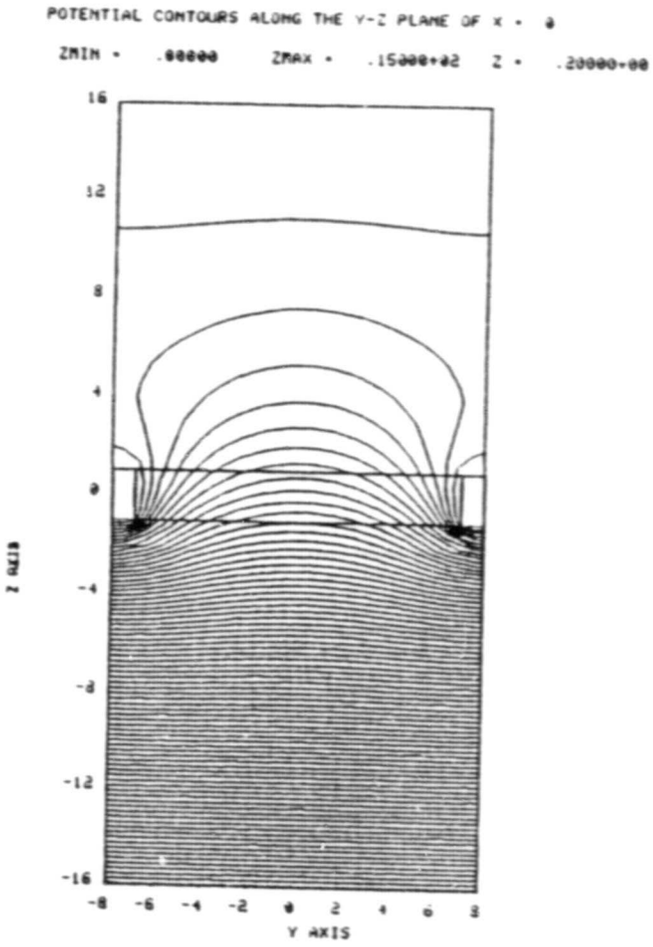

$\frac{\lambda}{d} = 8$

(75% TRANSPARENT)

Figure 4.5(a). Field penetration through cloth weave: 4% stray field above 77% transparent cloth.

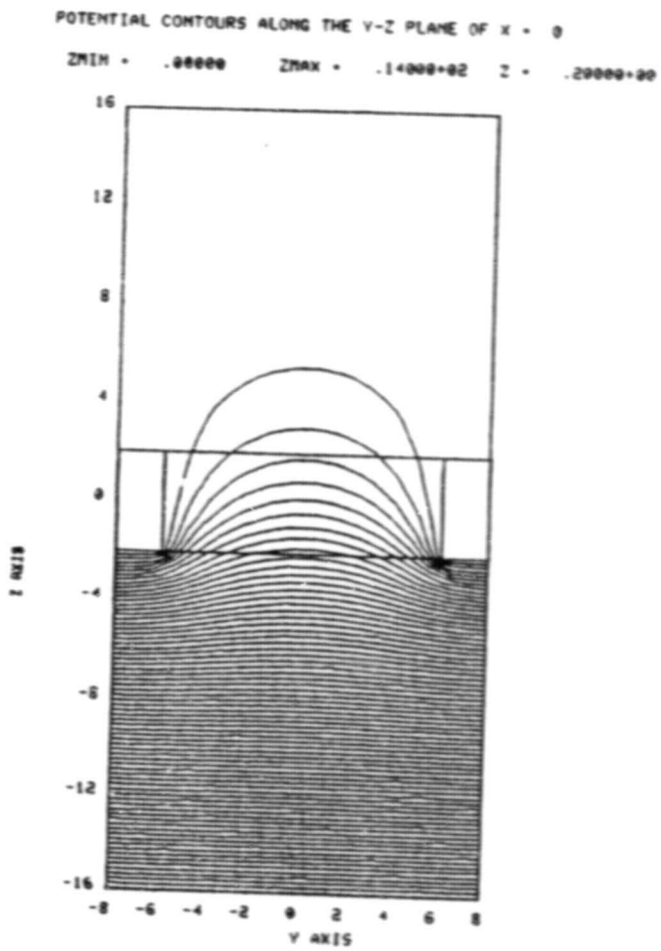

$\frac{\lambda}{d} = 4$

(50% TRANSPARENT)

Figure 4.5(b). Field penetration through cloth weave: 1% stray field above 56% transparent cloth.

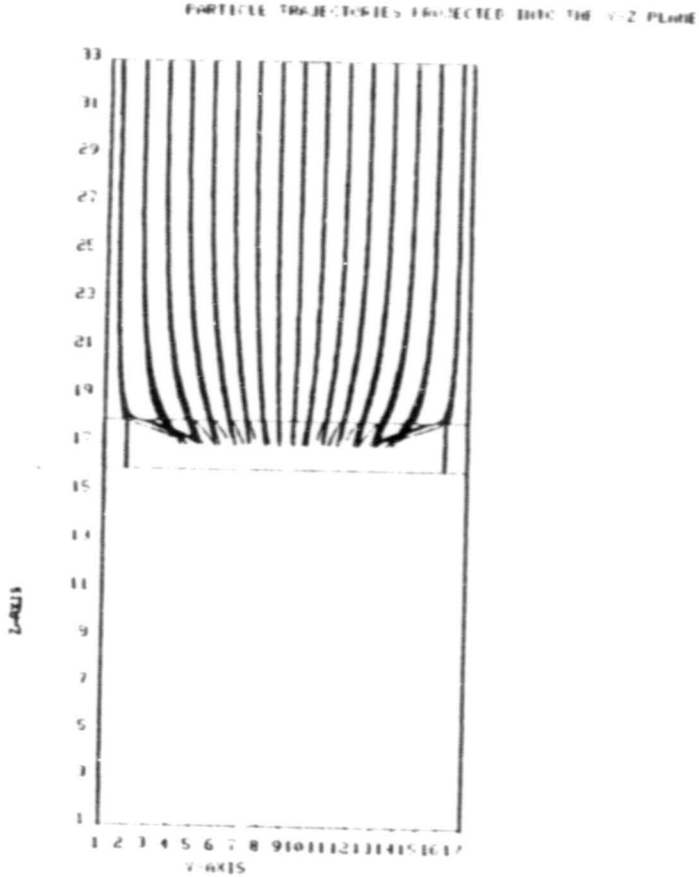

Figure 4.6(a). Particle focusing through cloth weave: 77% transparent ($\lambda/d = 8$).

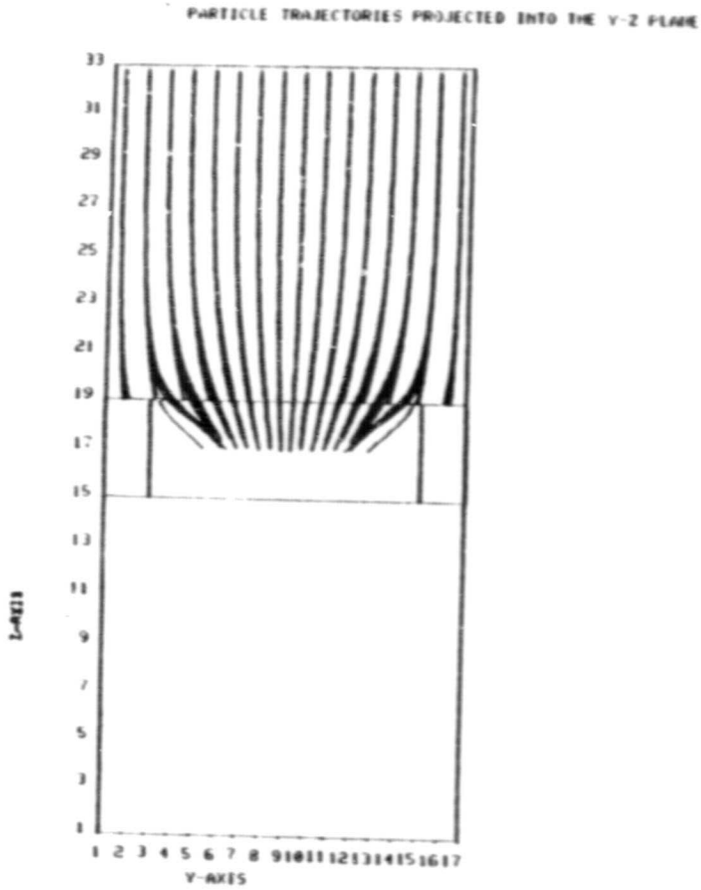

Figure 4.6(b). Particle focusing through cloth weave: 56% transparent ($\lambda/d = 4$).

Table 4.5. Summary of Cloth Potential and Particle Tracking Calculations		
Spacing/Diameter	8/1	4/1
Nominal Transparency	77%	56%
Field Leakage	4%	1%
Particle Transparency	98%	77%

4.5.3 Plasma Penetration Through the Plastic Membranes

The very thin (0.0003 to 0.0005 inch) membranes proposed for the ECCM will be penetrated by the high energy ($\varepsilon \gtrsim 20$ keV) electrons in the GEO plasma. While this sounds fairly high as a plasma temperature, half the current in a Maxwellian plasma has energy exceeding 1.7 times the temperature. Furthermore, a thermal characterization of the GEO plasma tends to underestimate the high energy plasma component.

Detailed theory and results for the power loss due to this mechanism are given in Appendix D. We find that, for a plasma density of 1 cm^{-3}, the power loss reaches 100 watts at a temperature of $\sim$10 keV for the 0.0003 inch membrane. Thus, the system design for an ECCM in GEO must allow for the fact that occasionally ($\lesssim$10 percent of the time) the antenna will require power in excess of 100 watts. A possible solution is to shut down the antenna when such a condition occurs. Such a solution, though painful, may be preferable to maintaining the surplus power needed to assure continuous operability.

This type of power loss can, in fact, be reduced by spacecraft charging. Due to the conducting design, it is unlikely that the structure will ever charge to negative potential in sunlight, since such potentials occur only as a consequence of differential charging.[18] In eclipse, however, negative potentials will be attained in the same environments which produce high power loss. We estimate that an aluminum surface will charge to -10 kV, and a kapton surface to -9 kV in a 10 keV environment. This will reduce the power loss by nearly a factor of three, and should reduce the frequency of shutdown to a tolerable level.

An interesting question is whether there are enough membrane-penetrating electrons in the LEO environment to cause substantial power loss. Even in the radiation belts (well above LEO) the current of high energy (>2 keV) electrons is less than 10^{-7} A/m^2, which would cause a power loss of only $\sim$50 W. Thus power loss due to high-energy electrons in LEO would be at most a few watts.

An additional possible power loss problem for these plastic membranes is back-side photoemission by transmitted ultraviolet. While we suspect that such photoemission is negligible, experimental verification would be worthwhile.

4.6 SPUTTERING

At altitudes of 200-300 km the velocity of a satellite in circular orbit is about 8×10^5 cm/sec. In the satellite frame of reference, ambient atomic oxygen and molecular nitrogen (or 0^+ and N_2^+) have kinetic energies of about 5 eV and 9 eV, respectively. Such energies must be only slightly above, if not below, the threshold for sputtering. Near threshold sputtering yields are not well known, but available measurements of sputtering show yields less than 10^{-2} at energies less than 1.5 times threshold.

Ion concentrations are of order $10^5/cm^3$ and neutral oxygen concentrations are about 10^9-10^{10} cm^{-3}. Assuming a yield of 10^{-2}, the time required to sputter a monolayer from a surface by species of concentration N (cm^{-3}) is

$$t_s \sim \frac{10^{15}}{8\times10^5 \times 10^{-2} N} \text{ sec}$$

10^6 sec (ions)

100 sec (atomic oxygen at 10^9 cm^{-3}) .

Thus, since the yield is not well known, sputtering of external surfaces by atomic oxygen in LEO poses a problem of uncertain proportions. Unless pertinent data on the sputtering of surfaces by 5 eV 0 atoms can be found, definitive experiments should be performed to assess the magnitude of the problem.

Ambient ion fluxes of about 10^{10} cm^{-2} sec^{-1} may reach a negatively biased electrode through any openings in the Faraday cage. Assuming that the sputtering yield for 50 KV ions is about 1, the time for monolayer removal is about 10^5 sec., or 1 day. Thus, one year or so would be required

to scrub 1000 Å of exposed areas of electrode surfaces, but the areas involved would be limited to about the size of the openings in the Faraday cage.

4.7 CONCLUSIONS

We conclude that, insofar as spacecraft-environment interactions are concerned, the electrostatically controlled membrane mirror (ECCM) is a viable concept for space applications. However, great care must be taken to enclose the high-voltage electrodes in a Faraday cage structure to separate the high-voltage region from the ambient plasma. For this reason, metallized cloth is not acceptable as a membrane material.

Conventional spacecraft charging at geosynchronous orbit should not be a problem provided ancillary structures (such as booms) are given non-negligible conductivity and adequate grounding. Arcing in the plastic membrane will probably occur occasionally for one-sided aluminization, and rarely for two-sided aluminization. However, loss of metallization sufficient to degrade antenna performance is highly unlikely.

Power loss due to plasma electrons entering the high-field region is a potentially serious problem. In low-earth orbit any opening whatever in the Faraday cage is likely to produce an unacceptable power drain. At geosynchronous altitude, where current levels are lower, a gap of $\sim$1 cm at the membrane point-of-attachment may be tolerable. However, a geosynchronous antenna will occasionally encounter high energy plasma capable of penetrating a thin membrane to produce power drains of one hundred watts or more. Provision must be made for shutting down the antenna during such periods.

The most credible sputtering problem is degradation of aluminized surfaces by ram neutrals in low-earth orbit. Even very low sputtering yields ($<10^{-2}$) can seriously damage these surfaces on a time scale of days or months. If pertinent data is not available, definitive experiments should be performed.

APPENDIX A

FLUID MODEL OF NEUTRALIZED ION BEAMS

by

D. E. Parks
M. J. Mandell
I. Katz

Systems, Science and Software
La Jolla, CA 92038

Paper AIAA-81-0141

Presented at

AIAA 19th Aerospace Sciences Meeting
January 12-15, 1981 - St. Louis, MO

FLUID MODEL OF NEUTRALIZED ION BEAMS

D. E. Parks, M. J. Mandell and I. Katz
Systems, Science and Software
La Jolla, California 92038

Abstract

The purpose of the present study is to determine the capability of a fluid model of electron transport to explain observed properties of ion thruster generated plasmas. Calculations reported here show that when the effective collision frequency in such a model is of the order of the electron plasma frequency, the resulting electric potential variations and electron temperatures are in qualitative agreement with values measured in the plasma generated by the SERT II thruster. Both theory and probe measurements made in flight and ground tests indicate substantial departures from the barometric law and strong variations of plasma potential across the beam boundary.

Nomenclature

$\vec{B}$	magnetic field
C	collision operator in Boltzmann-Vlasov equation
$\vec{E}$	electric field
$f_a d\vec{r}d\vec{v}$	number of particles of type a in phase space volume element dr dv at r,v
$\vec{\vec{F}}$	total energy flux
$\vec{F}_a$ =	$q_a(\vec{E} + \vec{v}\times\vec{B}/c)$
$\vec{\vec{I}}$	unit tensor
$\vec{J}$	net current density
k	Boltzmann's constant
m_a	mass of particle of species a
m	electron mass
n	electron density = $\int f(\vec{r},\vec{v},t)d\vec{v}$
p =	$1/3\ m \int f\ v'^2 d\vec{v}$ = scalar electron pressure
$\vec{\vec{p}}$	$m \int f\ \vec{v}'\vec{v}' d\vec{v} = p\vec{\vec{I}} + \vec{\vec{\pi}}$, pressure tensor
Q =	$1/2\ m\int v'^2 C\ d\vec{v}$
q_a	charge on particle of species a
q	magnitude of electron charge
$\vec{q}$	heat flux, Eq. (7)
$\vec{R}$	position vector of a particle
R =	$\int mv\ C\ dv$
T	electron temperature
$\vec{v}$	velocity of a particle
$\vec{v}'$ =	$\vec{v} - \vec{V}$
$\vec{V}$	mean or drift velocity = $1/n \int f(\vec{r},\vec{v},t)d\vec{v}$
λ_c	mean free path for pair collisions between electrons
Θ =	kT
η	plasma resistivity
κ	thermal conductivity of plasma
ν	effective collision frequency
ν_{ei}	electron-ion collision frequency
$\vec{\vec{\pi}}$ =	$nm\ \vec{v}\vec{v} - \langle v'^2\rangle/3\ \vec{\vec{I}}$ = stress tenson
σ =	η^{-1}
ϕ	electric potential
ω_p	electron plasma frequency

1. Introduction

The purpose of the present study is to determine the capability of a fluid model of electron transport to explain observed properties of ion thruster generated plasmas. Calculations reported here show that when the effective collision frequency in such a model is of the order of the electron plasma frequency, the resulting electric potential variations and electron temperatures are in qualitative agreement with values measured in the plasma generated by the SERT II thruster. Probe measurements made in SERT II[1] flight and ground test experiments[2] indicate substantial departures from the barometric law[3-7] and show strong variations of plasma potential across the beam boundary.

We propose to explain the plasma properties observed in the aforementioned experiments in terms of anomalous resistance of the plasma to the flow of electron current. The calculations are based on fluid equations expressing conservation of charge, momentum, and energy. We adopt the classical (ignoring thermoelectric effects) form of the equations of electron transport,[8] but permit reduced values of the transport coefficients. Predicted space dependent potentials, electron temperatures and current densities agree qualitatively with experimental results.

While the plasma is not collision dominated, randomization of electron velocities may still occur through enhanced levels of fluctuating fields, such as those initiated by streaming instabilities. Such fields are probably effective in coupling neutralizer electrons into the bulk plasma and in equalizing the mean drift of electrons with ions in the thruster beam. Such mechanisms are often approximated by introducing an effective collision frequency, ν.

Within a meter or so of the ion thruster, the electron densities are in the range

$$10^8 \leq n \leq 10^{13}\ cm^{-3}$$

and their velocity distribution is characterized by temperature Θ between about one and ten electron volts. The Debye length

$$\lambda_D \approx 700\sqrt{\frac{\Theta}{n}}\ cm$$

is typically small compared to distances L over which there is a substantial variation of macroscopic plasma properties such as density, potential, and temperatures. On the other hand, the mean free path for pair

collisions λ_c

$$\lambda_c \approx 10^{12}\, E^{1/2}\, \Theta^{1/2}/n \text{ cm}, \quad E \lesssim \Theta$$

for electrons of energy E (eV) is typically long compared to L, so that as previously asserted the behavior of the plasma is controlled by collective rather than collisional effects. Since $\lambda_D \ll L$, the plasma is quasineutral, departures from neutrality amounting roughly to

$$\delta n/n \sim \left(\frac{\lambda_D}{L}\right)^2 \sim 10^{-4} ,$$

the space around the vehicle is strongly shielded from surface potentials. This is in contrast to the situation that prevails in charging of spacecraft in geosynchronous orbit where effects of space charge are entirely negligible and potentials are determined as solutions of Laplace's equation.

Although collisionless, thruster-generated plasmas exhibit macroscopic behavior similar in many respects to that of a collisional plasma. Such behavior is perhaps not totally unexpected in view of the fact that in both non-equilibrium and equilibrium plasmas electrons are scattered by fluctuating electric fields. A primary difference between the equilibrium and non-equilibrium cases is in the magnitude of the fluctuating fields.

Several investigators have measured properties of thruster generated plasmas.[3-7] In the experiments of Ogawa, et al., on cesium ion beams neutralized by electrons from a hot wire, measurements were made of the density, potential, and electron temperature in the beam plasma. The potential difference between the neutralizer wire and the plasma could be varied by changing the position of the wire, the large potential differences (electron injection voltages) occurring when the wire was completely withdrawn from the beam plasma. An important result of the Ogawa experiments was that over a wide range of conditions electron density n and plasma potential ϕ were well correlated by the barometric law

$$n(\vec{r}) = \text{const} \exp(q\phi(\vec{r})/kT) \qquad (1)$$

The approximate validity of the barometric law was further verified by Kaufman.[7]

Since the barometric law is a thermal equilibrium concept, it can be completely valid only if the plasma is isothermal. The plasma is only approximately isothermal, noticeable deviation occurring as one proceeds from the beam axis beyond the beam edge into the plasma formed by ambient and charge exchange ions. Kaufman observes an electron temperature in the charge exchange plasma only about half that in the beam.[7] Ogawa[5] and Sellen[3] obtained measurable temperature variations in the beam plasma over several tens of centimeters in the downstream direction from the accelerator grid. The largest deviations from the barometric law were observed for large injection potentials ($\gtrsim$10 volts). Probe traces in such cases also indicated departures of the electron spectrum from a Maxwellian shape.

Probe measurements of the plasma potential in the thruster beam were made in SERT II flight and ground test experiments. The measurements show strong variation of plasma potential across the beam boundary about 20 cm downstream from the thruster grids. Such results are difficult to explain on the basis of a barometric law relationship unless the electron temperature or density variation from beam center to beam edge is much higher than might be expected from other measurements made in similar configurations. We anticipate, however, that such is not the case and, instead, that the observed behavior should be explained in terms of the anomolous resistivity of the thruster generated plasma to the flow of electron current. Thus, the primary objective of the following sections of the report is to determine the capability of simple transport models to explain, at least qualitatively, the experimental results.

The next section summarizes the kinetic equation for the electron distribution and the first few moment equations expressing conservation of charge, momentum, and energy. In Section 3 we state the approximations leading to the transport equations which we eventually solve. The method of solution and the results of calculations will be the subject of Sections 4 and 5 respectively. The final section, Section 6, summarizes the conclusions of this study.

2. Exact Equations for Electron Gas

In principle, a kinetic approach based on the Vlasov-Boltzmann equation fully describes the spacecraft generated plasma. The complexity of such an approach, however, makes it impractical as a basis for conducting multidimensional calculations of plasma behavior. Besides, except near sources and collecting surfaces, where the distribution function may change markedly, one should be able to adequately describe the plasma in terms of certain average properties of the distribution, such as temperature, density, and particle and heat fluxes. Below, the exact equations describing the plasma are given in order that the reader may be aware of the effects neglected in arriving at the approximate equations that are subsequently solved.

Quite generally the state of the plasma can be specified by the distribution function $f_a(\vec{r},\vec{v},t)$ that characterize each particle component a, where $f_a(\vec{r},\vec{v},t)d\vec{r}\,d\vec{v}$ represents the number of particles of species a in the six dimensional volume element $d\vec{r}\,d\vec{v}$ about the position $\vec{r},\vec{v}$ in phase space. The kinetic equations which

describe the distribution are

$$\frac{\partial f_a}{\partial t} + \vec{v}\cdot\nabla f_a + \frac{\vec{F}_a}{m_a}\cdot\nabla_v f_a = C_a \qquad (2)$$

For particles of mass m_a and charge q_a in an electric field $\vec{E}$ and a magnetic field $\vec{B}$ the "smoothed" force on a particle is $\vec{F}_a$. The effects of collisions between particles is taken account of by the collision term denoted here by C_a. Here we attempt to describe the plasma in terms of its density n, mean velocity $\vec{V}$, and certain higher velocity moments. For convenience, we have omitted the particle species subscript a. The first three moments of the kinetic equation yield conservation equations for particles, momentum and energy, as summarized below:[8]

Conservation of Particles

$$\frac{\partial n}{\partial t} + \nabla\cdot n\vec{V} = 0 \qquad (3)$$

Conservation of Momentum

$$\frac{\partial}{\partial t}(mn\vec{V}) + \nabla\cdot mn\vec{V}\vec{V} + \nabla\cdot\vec{\vec{P}} - qn\left(\vec{E} + \frac{\vec{V}\times\vec{B}}{c}\right) = \vec{R} \qquad (4)$$

Conservation of Energy

$$\frac{\partial}{\partial t}\left(\frac{nm}{2}\left(V^2 + \langle v'^2\rangle\right)\right) + \nabla\cdot\vec{F} = qnE\cdot V + \vec{R}\cdot\vec{V} + Q \qquad (5)$$

where

$$\vec{F} = \left[nm\left(\frac{V^2}{2} + \frac{\langle v'^2\rangle}{2}\right) + p\right]\vec{V} + \vec{\vec{\pi}}\cdot\vec{V} + \vec{q} \qquad (6)$$

is the total energy flux,

$$\vec{q} = nm\left\langle\frac{v'^2}{2}\right\rangle\vec{V} \qquad (7)$$

is the heat flux,

$$Q = \int \frac{mv'^2}{2} C\, d\vec{v} \qquad (8)$$

and $\langle\ \rangle$ denotes an average over the distribution f.

So far, the equations are quite general and involve no assumption that the gas is collision dominated or retains a Maxwellian spectrum of velocities. Separate conservation equations may be written not only for different particle species, but also for different groups or particles of the same charge and mass. Primary electrons, for example, with significant streaming energies could be treated as distinct from the main electron population which is taken to have a Maxwellian distribution of velocities. For the present, however, and until experimental or theoretical considerations dictate otherwise, we shall consider electrons as a whole and that their distribution varies slowly in space.

3. Approximations for Electron Gas

Consider that the plasma is in a steady state and that quasi-neutrality pertains throughout the bulk plasma (that is, away from electrodes and collecting surfaces). The electrons and ions each satisfy the particle continuity equation

$$\nabla\cdot n_i\vec{V}_i = 0 \quad (i = +,-) \qquad (9)$$

with $n_+ = n_- = n$. The momentum equation simplifies considerably if the electron drift velocity $\vec{V}$ is small compared to the random velocity $\langle v'^2\rangle^{1/2}$ and if the velocity distribution is nearly isotropic. Then, in the absence of magnetic fields,

$$\nabla p + en\vec{E} = \vec{R} \qquad (10)$$

where $\vec{R}$ represents the collisional drag between ions and electrons. In a classical plasma dominated by collisions, $\vec{R}$ is composed of a part proportional to the relative motion $\vec{u} = \vec{V}_e - \vec{V}_i$ between electrons and ions, leading to plasma resistivity, and to a thermal part proportional to the gradient of electron temperature, which is frequently neglected. In this approximation, equation (4) becomes

$$\nabla p + en\vec{E} = nne\vec{j} \qquad (11)$$

where $\vec{j}$ is the net current density and the plasma resistivity η is related to the electron-ion collision frequency ν_{ei} by

$$\eta^{-1} = \frac{\omega_p^2}{4\pi}\frac{1}{\nu_{ei}} \qquad (12)$$

If the plasma is non-resistive and isothermal, equation (11) yields the barometric law, equation (1). In this sense, equation (11), or more generally the complete electron momentum equation, may be regarded as the generalization of the barometric law.

If the plasma is not collision dominated, randomization of electron velocities may still occur through the enhanced levels of fluctuating fields in the plasma, such as occur for electron two-stream instabilities, or electron-ion instabilities of the ion-acoustic or Bunemann type.[8,9] These mechanisms are probably effective in coupling neutralizer electrons into the bulk plasma and in equalizing electron and ion mean drift velocities. They are often approximated by introducing an effective collision frequency, ν, in place of ν_{ei}.

The determination of electron temperatures in the plasma requires consideration of the energy balance equation, equation (5). Making the same approximations in the equation expressing conservation of energy that were made in the momentum equation, yields

$$\nabla\cdot\vec{F} = qn\vec{E}\cdot\vec{V} + \vec{R}_e\cdot\vec{V}_e + Q_{ei} \qquad (13)$$

with

$$\vec{F} = \frac{5}{2}\, p\vec{V} + \vec{q} \qquad (14)$$

Here 5/2 $p\vec{V}$ is the enthalpy flux of the drifting electrons, $\vec{q}$ the macroscopic heat flux, and $\vec{R}\cdot\vec{V}$ is related to the effective joule heating associated with the relative motion of electrons and ions. The quantity $\vec{R}$ appears also in the electron momemtum equation; for a plasma controlled by collective effects it should be approximated in the energy equation in the same manner as in the momentum equation. The heat flux, $\vec{q}$, contains new features. Classically, $\vec{q}$ contains two terms; one proportional to the relative drift velocity between electrons and ions, and the other proportional to the gradient of electron temperature.[8]

For the initial calculations, we ignore the drift contributions to the energy flux, the electron-ion heating Q_{ei}, and assume that the heat flux is proportional to the temperature gradient. The energy balance equation thus assumes the simple form

$$\nabla\cdot\kappa\nabla\Theta + mn\nu\,(\vec{v}_e-\vec{v}_i)^2 = 0 \qquad (15)$$

4. Ion Engine Neutralizer Code

The basic physics of an ion engine neutralizer model was presented in the preceding sections. This physical model has been incorporated into a two-dimensional (R-Z) computer code, which is described below. A sample calculation of neutralization in a thruster similar to SERT II is discussed below. Results are given for space dependent electric potentials, electron temperatures, and current densities.

Code Description

The ion thruster model has been incorporated into a two-dimensional (R-Z) computer code following the block diagram shown in Figure 1. For this initial version the ion currents and densities were assumed known. In a later version, it would be possible to allow a multicomponent ion composition to be determined self-consistently with the temperature and potential. The code operates entirely in MKS units.

The code has been run interactively, with all relevant information on disk file. As long as previous information exists on disk, the program may be entered from the two noted entry points as well as the beginning. For developmental purposes, it was found convenient to "hard-wire" many features of a particular problem into the code, while others are prompted for input. A flexible on-line graphics program, which plots information on the disk file, has also been developed.

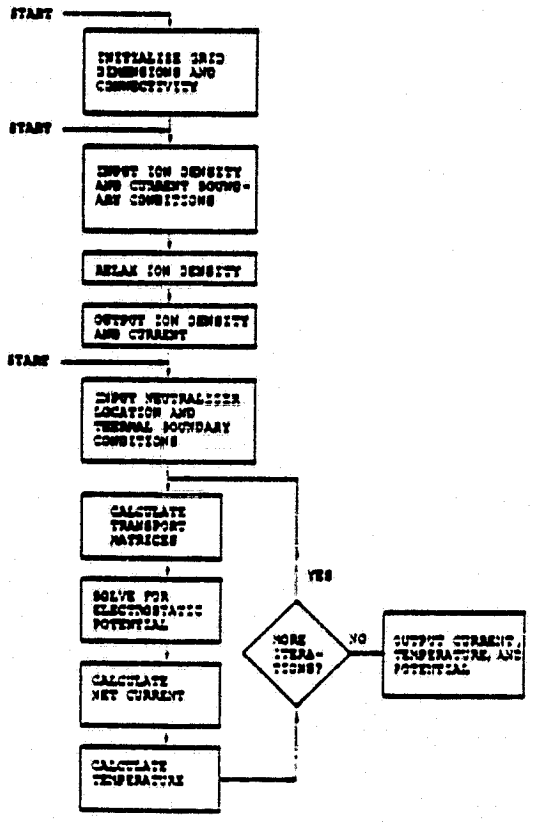

Fig. 1 Block diagram for ion engine neutralization code.

At present, the code assumes ion velocities everywhere and ion currents at the input boundary to be known. The code then calculates plasma densities such that $\nabla\cdot(n\underset{\sim}{v}) = 0$ is numerically satisfied. Typically, ion velocities are taken to be either purely axial or to be radial from a point source on the axis exterior to the mesh. As the code requires non-zero plasma density everywhere, a background density of "slow" ions may be added. It should be possible to handle multiple ion species with interconversion fairly easily.

The neutralizer is assumed to be a ring at specified distance from the axis, emitting a current of electrons equal to the ion beam current. The net current in the plasma is given by

$$\underset{\sim}{j} = nq(\vec{v}_i - \vec{v}_e) \qquad (16)$$

$$= \sigma\left(-\nabla\phi + \frac{q}{n}\nabla p\right), \qquad (17)$$

where now $p = nkT$ is the electron pressure. [For $\sigma\to\infty$ and $qkT\to\theta$ (constant) we find $\phi = \theta\ell n\, n$.] The code determines electrostatic potentials by solving $\nabla\cdot\underset{\sim}{j} = 0$. (See Appendix A.) It is necessary to iterate between this equation and the temperature equation (equation 15), since the pressure is a function of temperature.

The plasma temperature satisfies the equation

$$\nabla\cdot(-\kappa\nabla\theta) = \frac{j^2}{\sigma} \qquad (18)$$

where κ is the thermal conductivity and the right-hand-side represents the ohmic generation of heat. For this preliminary version, convective heat transport has been neglected. On the various boundary regions, either isothermal or insulating boundary conditions may be specified. Since, in practice, we take κ to have a power law dependence on θ, $\kappa = n\kappa'\theta^{n-1}$, the equation actually solved is

$$-\nabla\cdot\kappa'\nabla(\theta^n) = \frac{j^2}{\sigma} \quad . \qquad (19)$$

For convenience, the transport coefficients σ and κ' are calculated by a single isolated subroutine. The conductivity σ may depend on both density and temperature, and κ' on density only. The present version assumes a relaxation rate proportional to the plasma frequency:

$$\sigma = n^{1/2}\,\frac{e^2}{m}\,\frac{1}{8.98\alpha}\,, \qquad (20)$$

where the parameter α is taken to be 0.51. By the classical Weideman-Franz law,

$$\kappa = \frac{3}{2}\,\sigma\left(\frac{k}{q}\right)^2 T\,. \qquad (21)$$

If we measure temperature in eV, $k = q$, so that $\kappa' = 3/4\ \sigma$.

5. Computational Results

A calculation was performed for neutralization of a 0.23 ampere, purely axial beam of 3 keV mercury ions in a constant density background plasma. The beam had a radius of ∿7 cm, and a ring neutralizer was placed at a 17 cm radius. The given plasma density (Figure 2) had a peak of 16.1×10^{14} m^{-3}, and an ambient density of 1.0×10^{14} m^{-3}. These conditions approximate those occurring in the plasma produced by the SERT II thruster. The temperature profile (Figure 3) was calculated with insulating boundary conditions at the thruster. The maximum temperature occurs at the beam entrance, where the heat generation is greatest. The peak temperature was 5 eV, compared with a 1 eV assumed background. The electrostatic potentials are shown in Figures 4 and 5. Strong potential variations across the beam edge and a potential dip near the neutralizer are calculated features in qualitative agreement with experimental results (Figure 5).[11] While the strong edge fields conform approximately to the barometric law at the local temperature, they deviate substantially from the results that would be obtained with $\nu \ll \omega_p$ or by using the barometric law as the point of departure (that is, a zero resistivity, isothermal calculation). Current-vector plots (Figures 6 and 7) indicate that the beam is neutralized by electrons entering the beam from the side. The ion current is 50 percent neutralized at ∿15 cm downstream from the thruster.

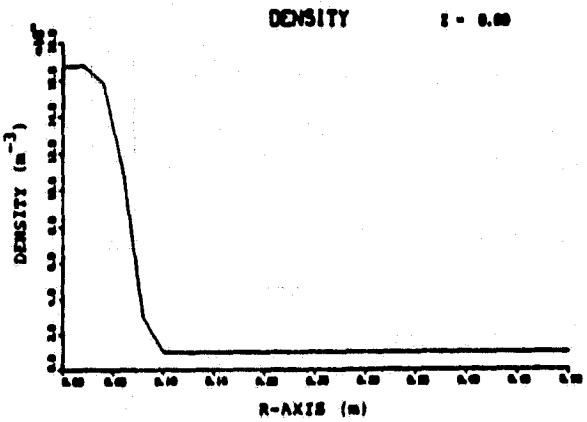

Fig. 2 Plasma density for SERT II ion thruster model.

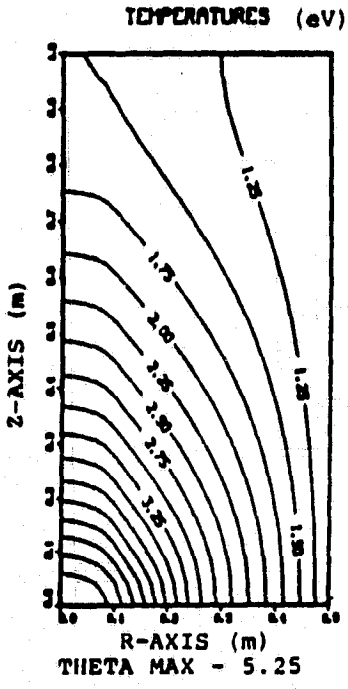

Fig. 3 Temperature profile for SERT II ion thruster model.

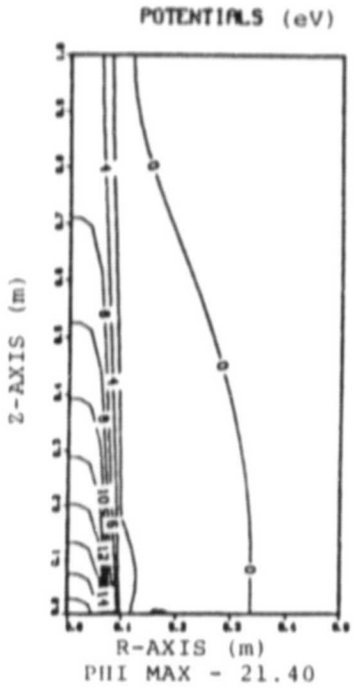

Fig. 4 Electrostatic potentials for SERT II ion thruster model.

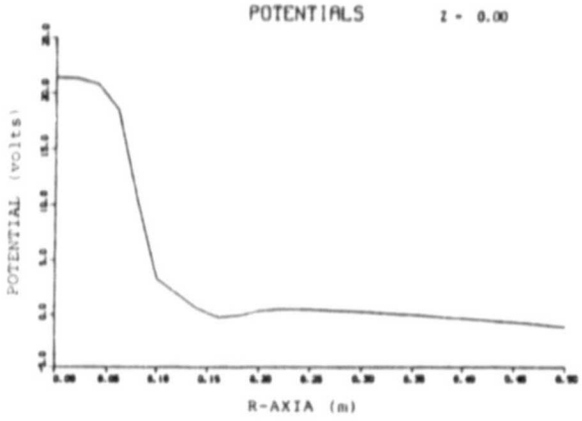

Fig. 5 Electrostatic potentials for SERT II ion thruster model.

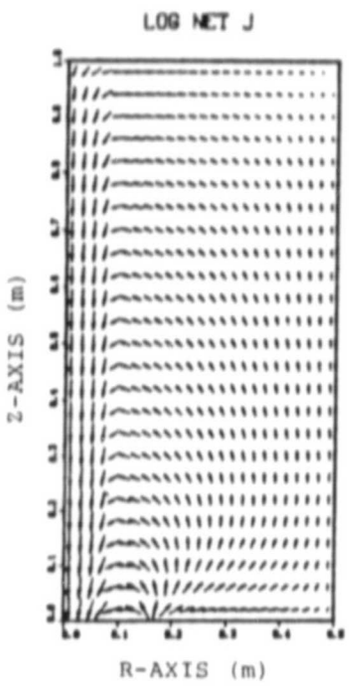

Fig. 6 Current vectors for SERT II ion thruster model. The length of each arrow is weakly dependent on current.

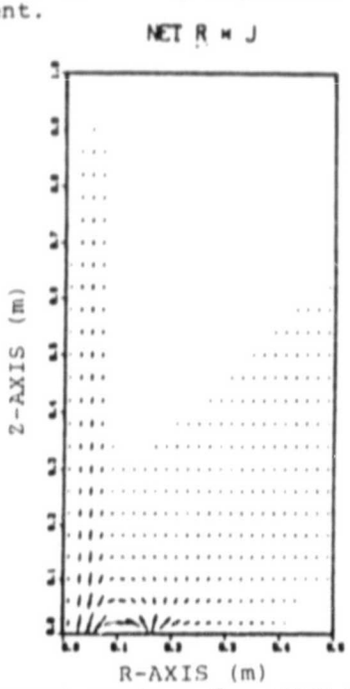

Fig. 7 Current vectors for SERT II ion thruster model. The length of each arrow is proportional to radius times current density.

6. Summary and Conclusions

The consequences of the assumption that the electron gas near an ion thruster behaves as a resistive fluid have been examined. Theoretical results obtained here are in qualitative agreement with experimental observations. Such agreement indicates that the properties of thruster

generated plasmas can be described by fluid equations having a classical form but with an effective collision frequency near ω_p, much in excess of the classical value for pair (electron-ion) collisions.

Further work should be performed to test qualitative and quantitative predictive capabilities of fluid models of thruster plasmas, and to better understand the relationship between ersatz fluid models of the type invoked here and the underlying plasma physical mechanisms embodied in the collisionless Vlasov equation.

Appendix A. Mathematical Considerations on the Variational Formulation of Poisson's Equation

In our theory of ion engine neutralization, it is necessary to solve equations of the form

$$\nabla\cdot[\sigma(\underset{\sim}{r})\nabla\phi] = S(\underset{\sim}{r}) \tag{A.1}$$

subject to fixed-value boundary conditions at some nodes and normal-gradient boundary conditions at others. We need to show that equation (A.1) is exactly the equation equivalent to the variational formulation, and that the normal-gradient boundary conditions are equivalent to a surface charge.

Theorem 1

Minimization of

$$\int_\Omega d^3\underset{\sim}{r}\left\{\frac{\sigma(\underset{\sim}{r})}{2}|\nabla\phi|^2 + \phi(\underset{\sim}{r})S(\underset{\sim}{r})\right\} \tag{A.2}$$

is equivalent to equation (A.1).

Proof

Minimization of $\int d^3\underset{\sim}{r}L(\phi,\nabla\phi,r)$ requires

$$\nabla\cdot\frac{\partial L(\phi,\nabla\phi,\underset{\sim}{r})}{\partial(\nabla\phi)} - \frac{\partial L(\phi,\nabla\phi,\underset{\sim}{r})}{\partial\phi} = 0 \tag{A.3}$$

Taking L as the integrand of (A.2), equation (A.3) yields exactly equation (A.1).

Theorem 2

In the finite-element formulation for the minimization of (A.2), normal-gradient boundary conditions are equivalent to surface charge.

Proof

In the finite-element formulation, minimization of (A.2) leads to the equations

$$\frac{\partial}{\partial\phi_i}\left\{\frac{1}{2}\sum_{jk}\phi_j W_{jk}\phi_k + \sum_\ell \phi_\ell S_\ell\right\} = 0 \tag{A.4}$$

where

$$W_{jk} = \int_\Omega d^3\underset{\sim}{r}\,\sigma(\underset{\sim}{r})[\nabla N_j(\underset{\sim}{r})]\cdot[\nabla N_k(\underset{\sim}{r})] \tag{A.5}$$

$$S_\ell = \int_\Omega d^3r\, N_\ell(r)\, S(\underset{\sim}{r}) , \tag{A.6}$$

$N_i(\underset{\sim}{r})$ are nodal interpolation functions and ϕ_i are node values for the unknown field.

Since $\underset{\sim}{W}$ is symmetric, these equations are

$$\sum_j W_{ij}\phi_j + S_i = 0 \tag{A.7}$$

Using (A.5) we find

$$\sum_j W_{ij}\phi_j = \int_\Omega d^3\underset{\sim}{r}[\nabla N_i(\underset{\sim}{r})]\cdot[\sigma(\underset{\sim}{r})\nabla\bar{\phi}(\underset{\sim}{r})] \tag{A.8}$$

where

$$\bar{\phi}(\underset{\sim}{r}) = \sum_i N_i(\underset{\sim}{r})\phi_i$$

The integrand of (A.8) can be rewritten as

$$\nabla\cdot[\sigma(\underset{\sim}{r})N_i(\underset{\sim}{r})\nabla\bar{\phi}(r)] - N_i(\underset{\sim}{r})\nabla\cdot[\sigma(r)\nabla\bar{\phi}(\underset{\sim}{r})] \tag{A.9}$$

Writing $\underset{\sim}{D}(\underset{\sim}{r}) = \sigma(r)\nabla\bar{\phi}(r)$, and using the divergence theorem, equation (A.7) becomes

$$\int_S d^2\underset{\sim}{r}\, N_i(\underset{\sim}{r})\,\underset{\sim}{D}(\underset{\sim}{r})\cdot\hat{n} - \int_\Omega d^3\underset{\sim}{r}\, N_i(\underset{\sim}{r})\,\nabla\cdot\underset{\sim}{D}(\underset{\sim}{r}) + S_i = 0 \tag{A.10}$$

where the first integral runs over the surface of volume Ω. By analogy with electrostatics, the second and third terms are the "volume charge" associated with node i, while the first, involving the surface-normal-gradient of the potential, is non-zero only on surface nodes and may be compensated by a corresponding surface-charge density.

Corollary

Consider the equation

$$\nabla\cdot J = 0 \tag{A.11a}$$

where

$$\underset{\sim}{J} = \sigma(\nabla\phi - g(\underset{\sim}{r})\nabla f) , \tag{A.11b}$$

and $f(\underset{\sim}{r})$, $g(\underset{\sim}{r})$ are known functions. If the inhomogeneous term is evaluated using equation (A.8), equation (A.11), with no further qualifications, will give zero-normal-current boundary conditions when solved by the finite-element method.

Furthermore, non-zero normal current boundary conditions, $\hat{n}\, J_B(r)$, can be invoked by adding an inhomogeneous term to the surface node equations.

Proof

Substituting (A.11) into (A.10), the finite element equations are

$$\int_S d^2\underset{\sim}{r}\; N_i(r)\; \underset{\sim}{J}(\underset{\sim}{r})\cdot\hat{n} - \int d^3\underset{\sim}{r}\nabla\cdot\underset{\sim}{J}(\underset{\sim}{r})\; N_i(\underset{\sim}{r}) = 0 \qquad \text{(A.12)}$$

As the second term is to vanish (within the finite-element approximation), it follows that the first term is equal to the right-hand-side. Thus, replacing the right-hand-side with

$$\int_S d^2\underset{\sim}{r}\; N_i(\underset{\sim}{r})\; J_B(\underset{\sim}{r}) \qquad \text{(A.13)}$$

will produce the specified boundary conditions.

References

1. Kerslake, W. R., D. C. Byers and J. F. Staggs, "SERT II: Mission and Experiments," J. Spacecraft 7, 1, p. 4, 1970.

2. Byers, David C. and John F. Staggs, "SERT: Thruster System Ground Testing," J. Spacecraft 7, 1, p. 7, 1970.

3. Sellen, J. M., Jr., W. Bernstein and R. F. Kemp, "Generation and Diagnosis of Synthesized Plasma Streams," Rev. Sci. Instr. 36, p. 316, 1965.

4. Bernstein, W. and J. M. Sellen, Jr., "Oscillations in Synthetic Plasma Beams," Phys. Fluids 6, p. 1032, 1963.

5. Ogawa, H. S., R. K. Cole and J. M. Sellen, Jr., "Factors in the Electrostatic Equilibration Between a Plasma Thrust Beam and the Ambient Space Plasma," AIAA Paper No. 70-1142, AIAA 8th Electric Propulsion Conference, 1970.

6. Ogawa, H. S., R. K. Cole and J. M. Sellen, Jr., "Measurements of Equilibration Potential Between a Plasma Thrust Beam and a Dilute Space Plasma," AIAA Paper No. 69-263, AIAA 7th Electric Propulsion Conference, 1969.

7. Kaufman, Harold R., "Interaction of a Solar Array with an Ion Thruster Due to the Charge-Exchange Plasma," NASA Report CR-135099, 1976.

8. Braginskii, S. I., Reviews of Plasma Physics, Vol. 1, Ed. M. A. Leontovich, Consultants Bureau, New York, p. 205, 1965.

9. Krall, Nicholas A. and Alvin W. Trivelpiece, Principles of Plasma Physics, McGraw-Hill, New York, 1973.

10. Bunemann, O., "Dissipation of Currents in Ionized Media," Phys. Rev. 115, p. 503, 1959.

11. Kerslake, W. R., private communication, NASA-Lewis Research Center, Cleveland, OH, November, 1979.

APPENDIX B

MATHEMATICAL CONSIDERATIONS ON THE VARIATIONAL FORMULATION OF POISSON'S EQUATION

In our theory of ion engine neutralization, it is necessary to solve equations of the form

$$\underset{\sim}{\nabla}\cdot[\sigma(\underset{\sim}{r})\underset{\sim}{\nabla}\phi] = S(\underset{\sim}{r}) \tag{B.1}$$

subject to fixed-value boundary conditions at some nodes and normal-gradient boundary conditions at others. We need to show that Eqn. (B.1) is exactly the equation equivalent to the variational formulation, and that the normal-gradient boundary conditions are equivalent to a surface charge.

Theorem 1

Minimization of

$$\int_{\Omega} d^3\underset{\sim}{r}\ \{\frac{\sigma(\underset{\sim}{r})}{2}|\underset{\sim}{\nabla}\phi|^2 + \phi(\underset{\sim}{r})S(\underset{\sim}{r})\} \tag{B.2}$$

is equivalent to Eqn. (B.1).

Proof

Minimization of $\int d^3\underset{\sim}{r} L(\phi,\underset{\sim}{\nabla}\phi,r)$ requires

$$\underset{\sim}{\nabla}\cdot\frac{\partial L(\phi,\underset{\sim}{\nabla}\phi,\underset{\sim}{r})}{\partial(\underset{\sim}{\nabla}\phi)} - \frac{\partial L(\phi,\underset{\sim}{\nabla}\phi,\underset{\sim}{r})}{\partial\phi} = 0 \tag{B.3}$$

Taking L as the integrand of (B.2), Eqn. (B.3) yields exactly Eqn. (B.1).

Theorem 2

In the finite-element formulation for the minimization of (B.2), normal-gradient boundary conditions are equivalent to surface charge.

Proof

In the finite-element formulation, minimization of (B.2) leads to the equations

$$\frac{\partial}{\partial \phi_i} \{\frac{1}{2} \sum_{jk} \phi_j W_{jk} \phi_k + \sum_{\ell} \phi_\ell S_\ell\} = 0 \qquad \text{(B.4)}$$

where

$$W_{jk} = \int_\Omega d^3\underset{\sim}{r}\, \sigma(\underset{\sim}{r}) [\nabla N_j (\underset{\sim}{r})] \cdot [\nabla N_k (\underset{\sim}{r})] \qquad \text{(B.5)}$$

$$S_\ell = \int_\Omega d^3 r\, N_\ell (r)\, S (\underset{\sim}{r}), \qquad \text{(B.6)}$$

$N_i(\underset{\sim}{r})$ are nodal interpolation functions and ϕ_i are node values for the unknown field.

Since $\underset{\sim}{W}$ is symmetric, these equations are

$$\sum_j W_{ij} \phi_j + S_i = 0 \qquad \text{(B.7)}$$

Using (B.5) we find

$$\sum_j W_{ij} \phi_j = \int_\Omega d^3\underset{\sim}{r}\, [\nabla N_i (\underset{\sim}{r})] \cdot [\sigma (\underset{\sim}{r}) \nabla\overline{\phi} (\underset{\sim}{r})] \qquad \text{(B.8)}$$

where

$$\overline{\phi} (\underset{\sim}{r}) = \sum_i N_i (\underset{\sim}{r}) \phi_i$$

The integrand of (B.8) can be rewritten as

$$\underset{\sim}{\nabla} \cdot [\sigma(\underset{\sim}{r}) N_i(\underset{\sim}{r}) \underset{\sim}{\nabla}\overline{\phi}(r)] - N_i(\underset{\sim}{r}) \underset{\sim}{\nabla} \cdot [\sigma(r) \underset{\sim}{\nabla}\overline{\phi}(\underset{\sim}{r})] \qquad (B.9)$$

Writing $\underset{\sim}{D}(\underset{\sim}{r}) = \sigma(r)\underset{\sim}{\nabla}\overline{\phi}(r)$, and using the divergence theorem, Eqn. (B.7) becomes

$$\int_S d^2\underset{\sim}{r}\, N_i(\underset{\sim}{r})\, \underset{\sim}{D}(\underset{\sim}{r})\cdot\hat{n} - \int_\Omega d^3\underset{\sim}{r}\, N_i(\underset{\sim}{r})\, \underset{\sim}{\nabla}\cdot\underset{\sim}{D}(\underset{\sim}{r}) + S_i = 0 \qquad (B.10)$$

where the first integral runs over the surface of volume Ω. By analogy with electrostatics, the second and third terms are the "volume charge" associated with node i, while the first, involving the surface-normal-gradient of the potential, is non-zero only on surface nodes and may be compensated by a corresponding surface-charge density.

Corollary

Consider the equation

$$\underset{\sim}{\nabla} \cdot \underset{\sim}{J} = 0 \qquad (B.11a)$$

where

$$\underset{\sim}{J} = \sigma(\underset{\sim}{\nabla}\phi - g(\underset{\sim}{r})\underset{\sim}{\nabla}f), \qquad (B.11b)$$

and $f(\underset{\sim}{r})$, $g(\underset{\sim}{r})$ are known functions. If the inhomogeneous term is evaluated using Eqn. (B.8), Eqn. (B.11), with no further qualifications, will give zero-normal-current boundary conditions when solved by the finite-element method. Furthermore, non-zero normal current boundary conditions, $\hat{n}\, J_B(r)$, can be invoked by adding an inhomogeneous term to the surface node equations.

Proof

Substituting (B.11) into (B.10), the finite element equations are

$$\int_S d^2\underset{\sim}{r}\; N_i(r)\; \underset{\sim}{J}(\underset{\sim}{r})\cdot\hat{n} - \int d^3r\; \underset{\sim}{\nabla}\cdot\underset{\sim}{J}(\underset{\sim}{r})\; N_i(\underset{\sim}{r}) = 0 \qquad (B.12)$$

As the second term is to vanish (within the finite-element approximation), it follows that the first term is equal to the right-hand-side. Thus, replacing the right-hand-side with

$$\int_S d^2\underset{\sim}{r}\; N_i(\underset{\sim}{r})\; J_B(\underset{\sim}{r}) \qquad (B.13)$$

will produce the specified boundary conditions.

APPENDIX C

ELECTRON PENETRATION OF THIN FILMS

A beam of electrons incident upon a solid surface will penetrate the material and undergo collisions with both its nuclei and electrons. The nuclear collisions lead to large angle scattering and attenuation of the beam in the incident direction. The electron scattering causes less deflection, but reduces the translational energy of the individual electrons. Eventually, when the energy of the incident, or primary, electrons has been reduced to (effectively) zero, they reach their maximum depth of penetration and stop. This maximum depth is called the "range." The range, R, is often considered to depend only upon the initial incident energy, E_o, and may be represented:

$$R = b_1 E_o^{n_1} + b_2 E_o^{n_2} \qquad (1)$$

Some of the energy absorbed by the material causes secondary electrons to be excited into conduction bands and to migrate to the surface and escape. For a material thick compared to the range, the escape-surface is always the same as the incident surface. An empirical theory of secondary emission is well established for this case.

The secondary electron yield, δ, (or ratio of secondary emitted to incident current) is given by the integral of the rate of production of secondaries at a depth x, multiplied by their probability of escape to the surface, over all x. The empirical theory employs the following model:

1. The rate of production of secondaries at a depth x is proportional to the rate of primary electron energy loss, or the "stopping-power" S(x), at that depth.

$$S(x) = \left|\frac{dE}{dx}\right| \quad . \tag{2}$$

2. The probability of escape of the secondaries once formed is proportional to $e^{-\alpha x}$, where α is a constant, and $1/\alpha$ is a characteristic "depth-of-escape" for each material.

The yield δ, for a normally incident beam is then given by:

$$\delta(0) = C \int_0^R S(x)\ e^{-\alpha x}\ dx \tag{3}$$

For a beam incident at an angle θ, the distance to the surface is no longer x, but $x\cos\theta$, i.e.

$$\delta(0) = C \int_0^R S(x)\ e^{-\alpha x\cos\theta}\ dx$$

Thin Films

For a film with a thickness on the same order as, or less than, the range, both secondary and primary electrons will be emitted from the back surface as well as the incident surface.

A central assumption in the empirical theory above is that secondary electrons are formed with isotropic initial velocities. Thus the probability of a secondary electron reaching the back surface has the same form as that for the front surface; i.e., proportional to $e^{-\alpha(T-x\cos\theta)}$ (Figure 1).

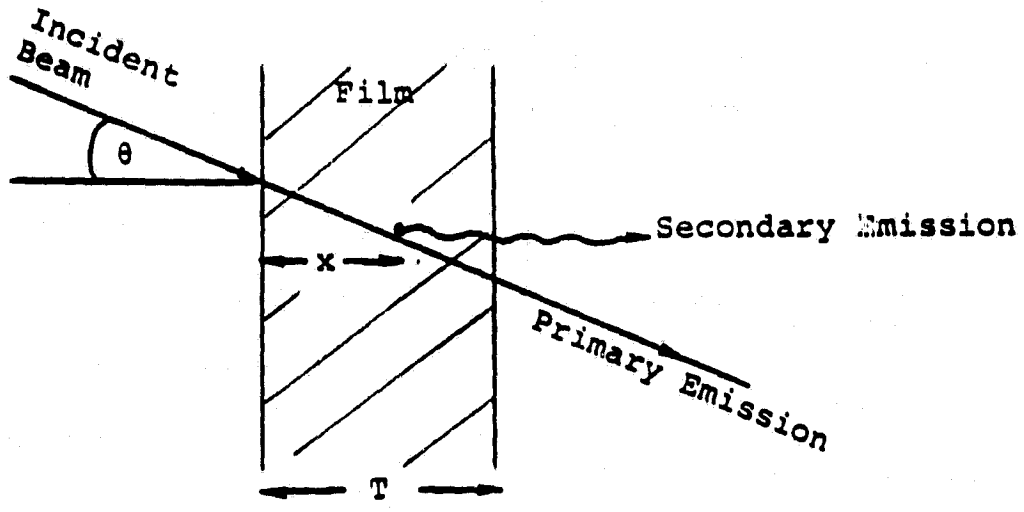

Figure 1.

The yield at the back surface is given by:

$$\delta^b(\theta) = C \int_0^R S(x)\, e^{-\alpha(T-x\cos\theta)}\, dx \qquad (4)$$

The fraction of primary electrons that are emitted from the back surface $\eta(\theta)$, is given by the transmission coefficient. This depends on the nuclear scattering and the beam attenuation, discussed above. The fraction of the incident beam scattered in the forward direction is given by $e^{-N\sigma x}$, where σ is the nuclear total scattering cross-section. σ depends on both the initial energy (and hence the range R – recall Eq. (1) – and the atomic number Z). Using the parameterized theory of Kanaga and Okayama (J. Phys. D. 5 43, 1972).

$$\eta(0) = e^{-0.187\, Z^{2/3}\, [x/(R-x)]} \qquad (5)$$

For a film of thickness T, the path-length for a beam, incident at an angle θ, through the film is $T/\cos\theta$.

$$\therefore \quad \eta(\theta) = e^{-0.187\, Z^{2/3}\, [T/(R\cos\theta - T)]} \tag{6}$$

The total current emitted through the back surface is the sum of the transmitted primary and secondary contributions.

$$i_{out} = i_{in}\, [\delta^b(\theta) + \eta(\theta)] \tag{7}$$

or, writing the total yield, $\tau(\theta)$ as:

$$\tau(\theta) = \delta^b(\theta) + \eta(\theta) \tag{8}$$

$$i_{out} = i_{in}\, \tau(\theta) \ . \tag{9}$$

In a more realistic space environment the electrons are derived from an isotropic plasma, with a Maxwellian distribution of initial energies E_o. In this case the total emitted current will be Eq. (9) averaged over all angles, and integrated over a Maxwellian distribution of initial energies.

$$\tau^{iso}(E_o) = 2 \int_0^1 \tau(\theta)\, \cos\theta\, d(\cos\theta) \tag{10}$$

$$i_{out}^{MAX} = FO \int_0^\infty \tau^{iso}(E_o)\, e^{-E_o/T} \tag{11}$$

where T is the temperature of the Maxwellian and

$$FO = N \left(\frac{T}{2\pi m}\right)^{1/2} \tag{12}$$

where N is the density and m is the electron mass.

Power Loss for an Aluminized Kapton Film

Calculation of the emitted current from the back surface of a film made of two materials A and B follows the above scheme very closely:

a. Secondary Yield

i. When the depth in the film D is less than the thickness T_A of the layer, A, presented first to the incident beam (outer).

$$S(x) = \left| \frac{dR^A(x)}{dE} \right|^{-1} \tag{13}$$

where $x = D/\cos\theta$.

$$\therefore \quad \delta(D) = C_A \, S(x) \, e^{-[\alpha_A (T_A - D) + \alpha_B T_B]} \tag{14}$$

ii. When D exceeds T_A, secondary production occurs in the second layer and:

$$S(x) = \left| \frac{dR^B(x)}{dE} \right|^{-1} \tag{15}$$

where we calculate the remaining energy upon entering $B(E_{OB})$ via the range formula in A.

$$n_1^A \, b_1^A \, E_{0B}^{(n_1^A - 1)} + n_2^A \, b_2^A \, E_{0B}^{(n_2^A - 1)} = R_A - (T_A/\cos\theta) \tag{16}$$

$$\therefore \quad \delta(D) = C_B \, S(x) \, e^{-\alpha_B (T_B - D)} \tag{17}$$

b. Transmission Coefficient

To be transmitted the range R must exceed the total distance traveled inside the film, $x = T/\cos\theta$, where $T = T_A + T_B$, the total thickness of the film. The range, R, is calculated in two parts.

i. Layer A

If R_A, calculated from (1) exceeds $x_A = T_A/\cos\theta$, the electron will proceed into layer B with energy E_{0B} given by (16) above. The fraction of the incident beam entering layer B is η_A

$$\eta_A = e^{-0.187\ Z^{2/3}\ [T_A/(R_A \cos\theta - T_A)]} \tag{18}$$

ii. Layer B

The range in layer B, R_B, is given by the range formula using E_{0B}, as the initial energy. The fraction transmitted η_B is calculated via (18) above.

The overall transmission coefficient is then

$$\eta = \eta_A \times \eta_B \tag{19}$$

Integrating over an isotropic Maxwellian gives the overall emitted current per unit area. For a 100 m diameter disk, above a +50 keV potential, the total power loss will be:

$$P = i_{out}^{iso} \cdot \pi \cdot \left(\frac{100}{2}\right)^2 \cdot 50 \times 10^3\ W$$

Results

Using the above formulation the yields for a series of monoenergetic beams and the power losses for a series of Maxwellian environments were calculated for the following 100 m diameter disks of films:

1. 0.3 mil (∿75,000 Å) Kapton coated with ∿350 Å of Aluminum, with the Kapton facing the incident beam.
2. 0.5 mil (∿125,000 Å) Kapton coated with ∿350 Å of Aluminum, again with the Kapton on the incident surface.

The yields and power losses are tabulated below.

TRANSMISSION YIELDS

0.3 mil (75,000 Å) Kapton Backed with 350 Å Aluminum

Energy (keV)	Secondary	Primary	Total
22	0	0	0
24	0.063	0.0016	0.064
26	0.078	0.028	0.11
28	0.082	0.085	0.17
30	0.078	0.16	0.23
32	0.074	0.23	0.30
34	0.073	0.30	0.37
36	0.070	0.36	0.43
38	0.067	0.42	0.48
40	0.064	0.47	0.53
50	0.049	0.65	0.70
75	0.038	0.84	0.88
100	0.025	0.91	0.94

POWER LOSSES

0.3 mil (75,000 Å) Kapton Backed with 350 Å Aluminum

Density = 1.0 cm^{-3}

Temperature (keV)	Incident Current (μ Am^{-2})	Emitted Current (μ Am^{-2})	Power Loss (W)
4	1.7	0	0
6	2.1	0.042	16
8	2.4	0.16	61
10	2.7	0.32	120
12	2.9	0.52	200
14	3.2	0.75	300
16	3.4	0.99	390
18	3.6	1.2	490
20	3.8	1.5	590
30	4.6	2.7	1000
50	6.0	4.5	1800

TRANSMISSION YIELDS

0.5 mil (125,000 Å) Kapton Backed with 350 Å Aluminum

Energy (keV)	Secondary	Primary	Total
28	0	0	0
30	0.023	0	0.023
32	0.053	0.001	0.054
34	0.063	0.018	0.080
36	0.064	0.053	0.12
38	0.065	0.10	0.17
40	0.064	0.15	0.22
50	0.053	0.40	0.46
75	0.035	0.72	0.76
100	0.026	0.84	0.87

POWER LOSSES

0.5 mil (125,000 Å) Kapton Backed with 350 Å Aluminum

Density = 1.0 cm^{-3}

Temperature (keV)	Incident Current (μ Am^{-2})	Emitted Current (μ Am^{-2})	Power Loss (W)
6	2.1	0	0
8	2.4	0.043	17
10	2.7	0.13	52
12	2.9	0.25	100
14	3.2	0.41	160
16	3.4	0.58	230
18	3.6	0.78	300
20	3.8	0.99	390
30	4.6	2.0	800
50	6.0	3.9	1500

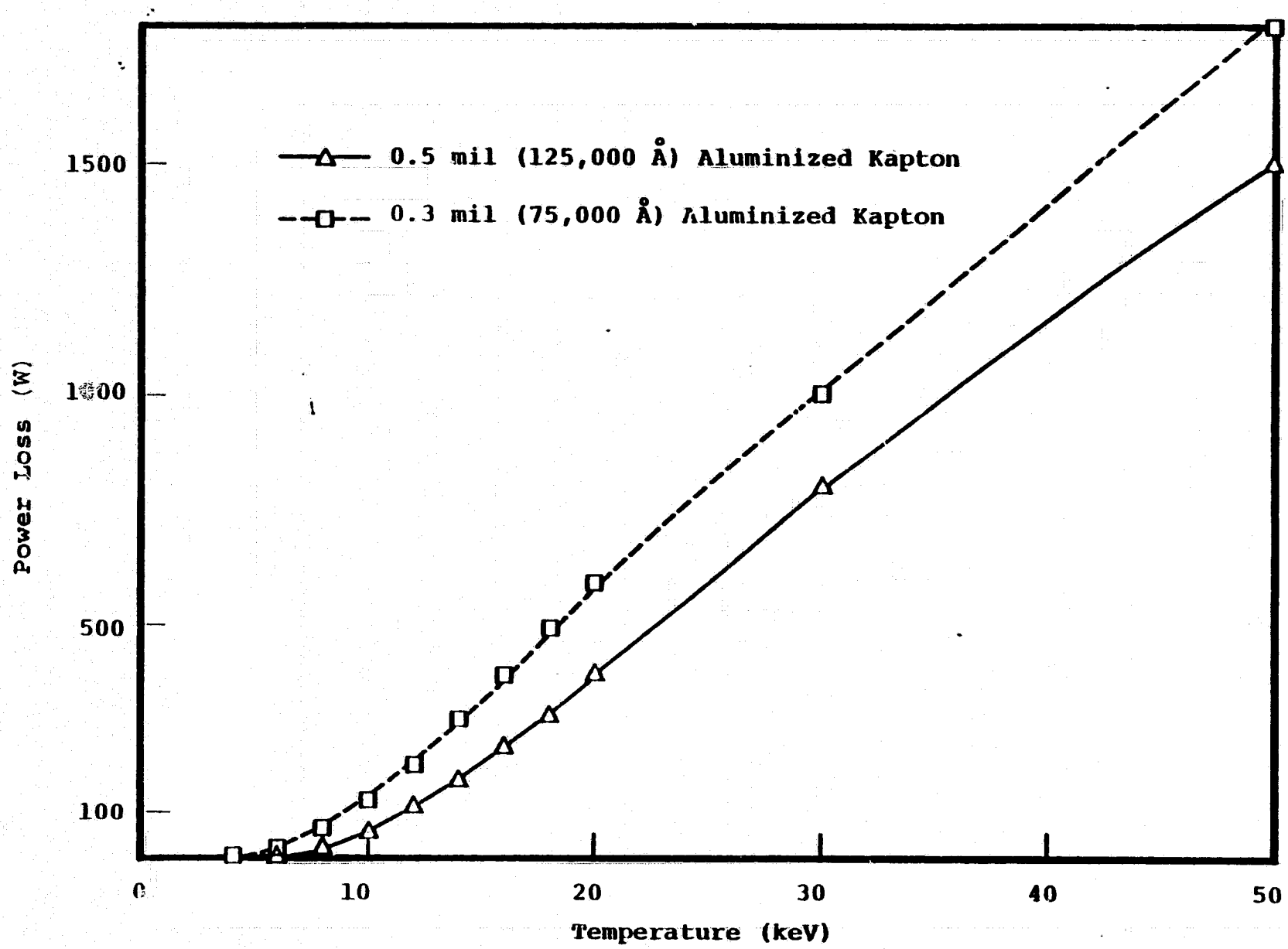

POWER LOSSES FOR 1.0 cm^{-3} DENSITY MAXWELLIANS

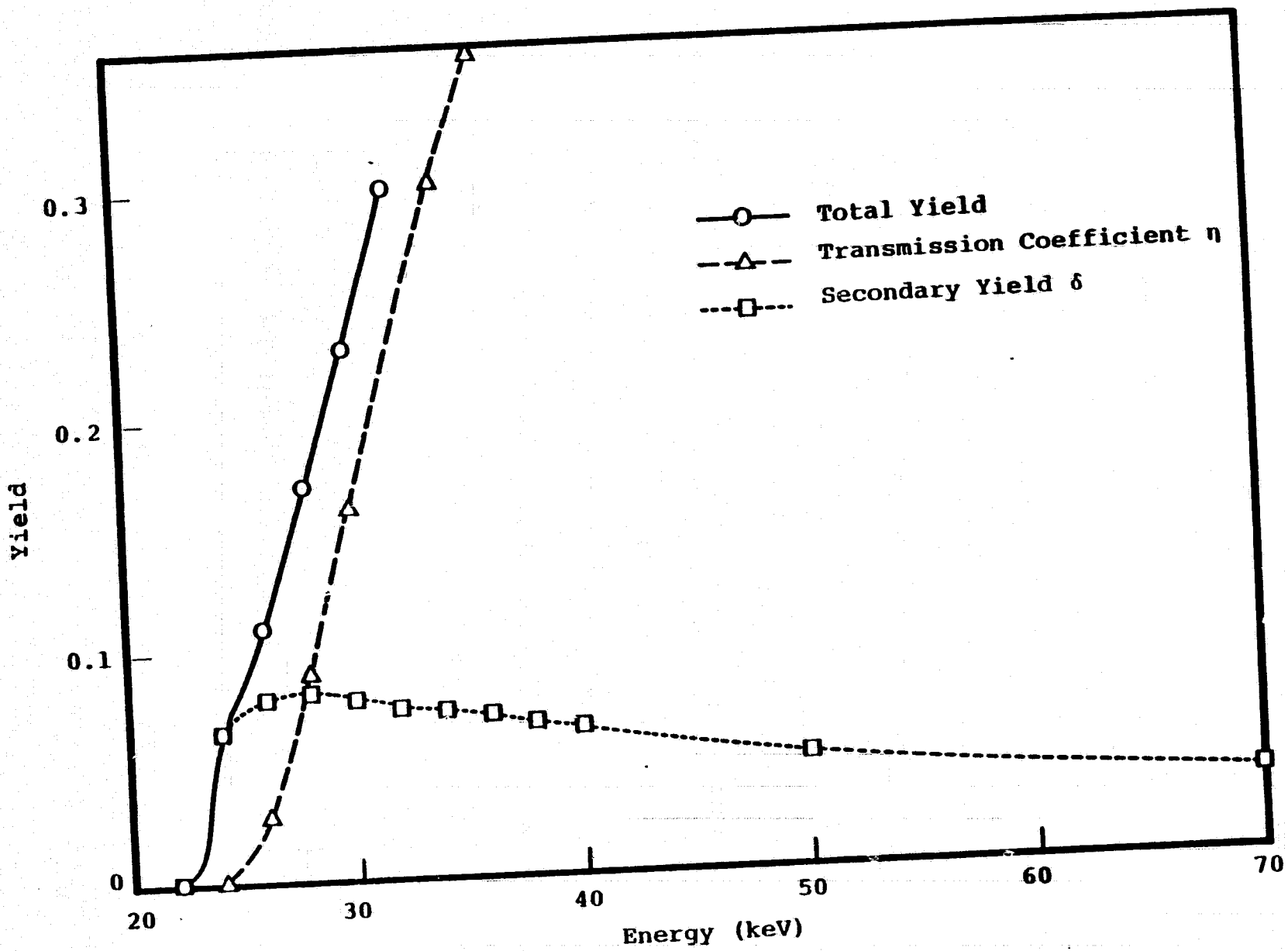

TRANSMISSION YIELDS FOR 0.3 mil ALUMINIZED KAPTON

APPENDIX

Computer Code LEAK

To calculate electron penetration and power loss through a general two-material film, a small code (LEAK) has been written and has the following features:

1. Subroutines

   a. LEAK - the main program.

   b. TRASEC - calculates the transmitted secondary yield. TRASEC has the same argument list as ELSEC, etc., in MATCHG and NASCAP.

   c. TRANIT - calculates the transmission coefficient, and has the same format as TRASEC.

   d. DELC - calculates the integrand for the numerical integration in TRASEC.

   e. TCOEF - calculates the integrand for the angular integration in TRANIT.

   f. STOP - solves the stopping power equation (16) for E_{OB} and the stopping power.

   g. RANGE - calculates the range for each material given an initial energy.

   h. MAXWSR - integrates the yield over a Maxwellian. Identical to NASCAP and MATCHG routines.

2. Input

   The present version is fixed to calculate yields only for isotropic incident electrons and power losses only for 100 m diameter disks above a +50 keV potential. A more flexible version is trivial to achieve if required.

   a. DATA INPUT - The four range parameters of each material and their secondary emission parameters (C, α) are supplied in a DATA statement.

b. INTERACTIVE INPUT

- thickness of incident layer.
- thickness of emitting layer.
- temperature step size (T-keV). (20 values of output variables are determined at temperatures T, 2T... 20T.)
- the density of the Maxwellian (N, m-3).
- the film potential in volts.

3. Output

Two tables are produced:

a. A table of secondary, primary, and total yields for monoenergetic beams of electrons. The energies are given by T, 2T...20T.

b. A table of incident and emitted current and power loss for Maxwellian environments with density N and temperatures T, 2T...20T.

The program and subroutines are in file STANNARD-P*ANT.

APPENDIX D

APPROXIMATE CALCULATION OF ENHANCEMENT OF GAP AREA FOR ELECTROSTATIC ANTENNA

In construction the electrostatically - controlled membrane minor (ECCM), it maybe desirable to leave a small (~1cm) gap at the point of attachment. If this gap is at high potential relative to the nearby election plasma, its effective current collection area will be far in excess of its nominal area. In this note we provide a rough estimate of this enhancement factor.

A. ESTIMATE OF GAP POTENTIAL

Consider the geometry of figure 1.

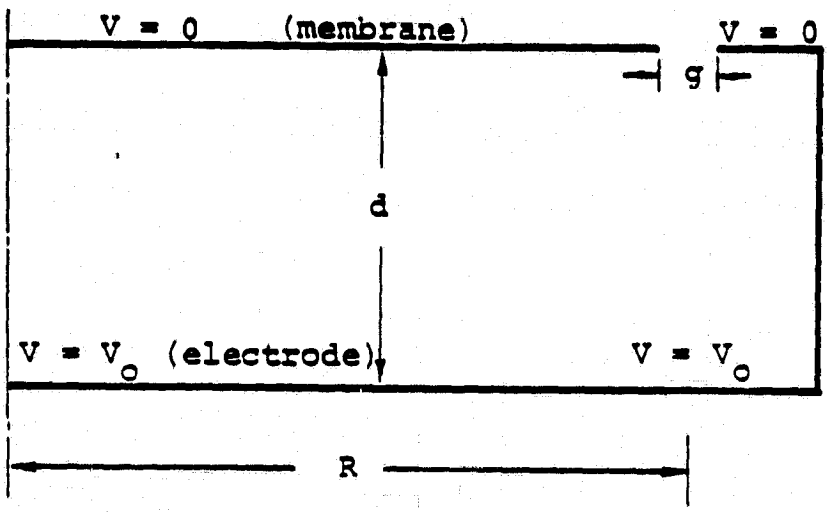

Figure 1.

We will estimate the potential, V_G, at the center of the gap (width g) by minimizing an approximation to the electrostatic energy per unit length of gap, $U/2\pi R$, where

$$U = \frac{\epsilon_o}{2} \int d^3\underset{\sim}{r} \; |E|^2 \; .$$

(Minimizing the electrostatic energy is equivalent to solving Laplace's equation).

The electric field may be regarded as a superposition of the field in the absence of the gap ($E = V_o/d$ below the

membrane; E = 0 above) with the field due to the gap potential on an otherwise grounded system. To estimate the latter we write the surface potential in the gap region as a Fourier sum

$$\phi(r) = \sum_{\ell} \phi_{\ell} \cos K_1 \ell r.$$

Since each component dies exponentially in z:

$$\phi(r,z) = \sum_{\ell} \phi_{\ell} e^{-K_1 \ell z} \cos K_1 \ell r$$

the longest wavelength ($K_1 = \pi/g$) dominates. Thus we approximate the gap field by $V_G/(g/\pi)$ through a volume $2\pi R\ (g/\pi)^2$.

The change in electrostatic energy is given by:

$$\frac{\Delta U}{2\pi R} \approx (g/\pi)^2\ (\varepsilon_o/2) \left\{ \left[\left(\frac{V_o}{d} - \frac{\pi V_G}{g} \right)^2 - \left(\frac{V_o}{d} \right)^2 \right] + \left[\left(\frac{\pi V_G}{g} \right)^2 \right] \right\}$$

when the first square bracket gives the decrease in energy below the membrane and the second the increase above. Minimizing this expression gives

$$V_G = \frac{V_o}{2\pi} \frac{g}{d} .$$

B. ENHANCED COLLECTION AREA

The effective collecting surface (assumed approximately circular) is shown in figure 2. Its height, h, is the distance

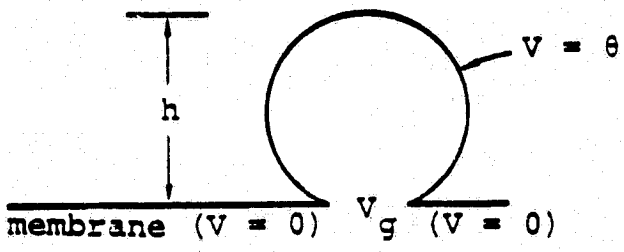

Figure 2.

in which the perturbation potential due to the gap is comparable to the plasma temperature, θ. Thus

$$\theta = V_G \, e^{-\pi h/g}$$

and

$$A_{eff} = (2\pi R)\ (\pi h).$$

Combining these results, we have

$$A_{eff} = 2\pi R g \left[\ln \left(\frac{V_o}{\theta} \ \frac{g}{2\pi d} \right) \right].$$

Note that the enhancement factor (in square brackets) is only a logarithmic function of the constants in the problem, and thus not overly sensitive to the approximations used to make this estimate.

Example

In GEO the dominant plasma near a spacecraft is the satellite's own photoelectrons, for which $\theta \sim 1$eV. If $V_o = 50$keV, $g = 1$ cm, $d = 10$ cm, the area enhancement factor is 6.7. Since the photocurrent is $\sim 2 \times 10^{-5}$ A/m^2, the power loss for a 100m diameter membrane is:

Power loss $= 6.7 \times 2\pi \times 50 \times .01 \times (2 \times 10^{-5}) \times (5 \times 10^4)$

$= 21$ watts

REFERENCES

1. Katz, I., et al., "Additional Application of the NASCAP Code. Volume I – NASCAP Extension," NASA CR-165349, February 1981.

2. Parks, D. E. and I. Katz, "Spacecraft-Generated Plasma Interaction with High-Voltage Solar Array," J. Spacecraft and Rockets, Vol. 16, No. 4, July-August 1979.

3. Poeschel, R. L., et al., "Extended Performance Solar Electric Propulsion Thrust System Study," NASA CR-135281, 1977.

4. Katz, I., M. J. Mandell, G. W. Schnuelle, D. E. Parks and P. G. Steen, "Plasma Collection by High Voltage Spacecraft at Low Earth Orbit," AIAA 18th Aerospace Sciences Meeting, AIAA-80-0042, January 14-16, 1980, Pasadena, CA.

5. Mandell, M. J., I. Katz, P. G. Steen and G. W. Schnuelle, "The Effect of Solar Array Voltage Patterns on Plasma Power Losses," IEEE Conference on Nuclear and Space Radiation Effects, July 1980, Ithaca, NY.

6. Sellen, J. M., Jr., W. Bernstein and R. F. Kemp, "Generation and Diagnosis of Synthesized Plasma Streams," Rev. Sci. Instr., Vol. 36, 316, 1965.

7. Bernstein, W. and J. M. Sellen, Jr., "Oscillations in Synthetic Plasma Beams," Phys. Fluids, Vol. 6, 1032, 1963.

8. Ogawa, H. S., R. K. Cole and J. M. Sellen, Jr., "Factors in the Electrostatic Equilibration Between a Plasma Thrust Beam and the Ambient Space Plasma," AIAA 70-1142, AIAA 8th Electric Propulsion Conference, 1970.

9. Ogawa, H. S., R. K. Cole and J. M. Sellen, Jr., "Measurements of Equilibration Potential Between a Plasma Thrust Beam and a Dilute Space Plasma," AIAA 69-263, AIAA 7th Electric Propulsion Conference, 1969.

10. Kaufman, H. R., "Interaction of a Solar Array With an Ion Thruster Due to the Charge-Exchange Plasma," NASA CR-135099, 1976.

11. Braginskii, J. I., Reviews of Plasma Physics, Vol. 1, Ed. M. A. Leontovich, Consultants Bureau, New York, 205, 1965.

12. Krall, N. A. and A. W. Trivelpiece, Principles of Plasma Physics, McGraw-Hill, New York, 1973.

13. Bunemann, O., "Dissipation of Currents in Ionized Media," Phys. Rev., 115, 503, 1959.

14. Siegfried, D. E. and P. J. Wilbur, "An Investigation of Mercury Hollow Cathode Phenomena," AIAA/DGLR 13th International Electric Propulsion Conference, Paper 78-705, 1978.

15. Mihora, D. J. and P. J. Redmond, "Electrostatically Focused Antennas," AIAA 79-0922.

16. Garrett, H. B., "Review of Quantitative Models of the 0- to 100-keV Near-Earth Plasma," Rev. Geophysics and Space Physics, 17, 397, 1979.

17. Valley, S. L., Handbook of Geophysics and Space Environments, 6.1-6.2, 1965.

18. Mandell, M. J., I. Katz, G. W. Schnuelle, P. G. Steen and J. C. Roche, "The Decrease in Effective Photocurrents Due to Saddle Points in Electrostatic Potentials Near Differentially Charged Spacecraft," IEEE Trans. Nucl. Sci., NS-25, 1313, 1978.